The EUV Imaging Spectrometer for Hinode

**J.L. Culhane · L.K. Harra · A.M. James · K. Al-Janabi · L.J. Bradley ·
R.A. Chaudry · K. Rees · J.A. Tandy · P. Thomas · M.C.R. Whillock · B. Winter ·
G.A. Doschek · C.M. Korendyke · C.M. Brown · S. Myers · J. Mariska · J. Seely ·
J. Lang · B.J. Kent · B.M. Shaughnessy · P.R. Young · G.M. Simnett · C.M. Castelli ·
S. Mahmoud · H. Mapson-Menard · B.J. Probyn · R.J. Thomas · J. Davila · K. Dere ·
D. Windt · J. Shea · R. Hagood · R. Moye · H. Hara · T. Watanabe · K. Matsuzaki ·
T. Kosugi · V. Hansteen · Ø. Wikstol**

T. Kosugi deceased 2006 November 26.

J.L. Culhane (✉) · L.K. Harra · A.M. James · K. Al-Janabi · L.J. Bradley · R.A. Chaudry ·
K. Rees · J.A. Tandy · P. Thomas · M.C.R. Whillock · B. Winter
Mullard Space Science Laboratory, University College London, Holmbury St Mary, Dorking,
Surrey, RH5 6NT, UK
e-mail: jlc@mssl.ucl.ac.uk

G.A. Doschek · C.M. Korendyke · C.M. Brown · S. Myers · J. Mariska · J. Seely
Naval Research Laboratory, E.O. Hulburt Centre for Space Research, Washington, DC 20375-5320,
USA

J. Lang · B.J. Kent · B.M. Shaughnessy · P.R. Young
Space Science and Technology Department, Rutherford Appleton Laboratory, Chilton, Didcot,
Oxfordshire, OX11 0QX, UK

G.M. Simnett · C.M. Castelli · S. Mahmoud · H. Mapson-Menard · B.J. Probyn
Space Research Group, School of Physics and Space Research, University of Birmingham,
Birmingham, UK

R.J. Thomas · J. Davila
NASA Goddard Space Flight Centre, Code 682, Greenbelt, MD 20771, USA

K. Dere
School of Computational Sciences, George Mason University, 4400 University Drive, Fairfax,
VA 22030, USA

D. Windt
Pupin Physics Laboratories, Department of Astronomy, Columbia University, 550 West 120th
Street, New York, 10027, USA

J. Shea
Perdix Corporation, P.O. Box 23, 35 Howard Street, Wilton, NH 03086, USA

R. Hagood
Swales Aerospace, 5050 Powder Mill Road, Beltsville, MD 20705, USA

Abstract The EUV Imaging Spectrometer (EIS) on Hinode will observe solar corona and upper transition region emission lines in the wavelength ranges $170 - 210$ Å and $250 - 290$ Å. The line centroid positions and profile widths will allow plasma velocities and turbulent or non-thermal line broadenings to be measured. We will derive local plasma temperatures and densities from the line intensities. The spectra will allow accurate determination of differential emission measure and element abundances within a variety of corona and transition region structures. These powerful spectroscopic diagnostics will allow identification and characterization of magnetic reconnection and wave propagation processes in the upper solar atmosphere. We will also directly study the detailed evolution and heating of coronal loops. The EIS instrument incorporates a unique two element, normal incidence design. The optics are coated with optimized multilayer coatings. We have selected highly efficient, backside-illuminated, thinned CCDs. These design features result in an instrument that has significantly greater effective area than previous orbiting EUV spectrographs with typical active region $2 - 5$ s exposure times in the brightest lines. EIS can scan a field of 6×8.5 arc min with spatial and velocity scales of 1 arc sec and 25 km s^{-1} per pixel. The instrument design, its absolute calibration, and performance are described in detail in this paper. EIS will be used along with the Solar Optical Telescope (SOT) and the X-ray Telescope (XRT) for a wide range of studies of the solar atmosphere.

1. Introduction

The Hinode mission will study the Sun at visible, EUV and X-ray wavelengths. Visible observations will be made with a 0.5 m diffraction-limited telescope — the largest solar optical instrument yet deployed in space. The Solar Optical Telescope (SOT), constructed by NAOJ and Lockheed-Martin, will investigate photospheric dynamics and make vector magnetogram maps at $\approx$0.25 arc sec (175 km) resolution.

X-ray observations will be made with a grazing incidence X-Ray Telescope (XRT) having 2 arc sec spatial resolution. Constructed by Smithsonian Astrophysical Observatory and NAOJ, it images the entire solar atmosphere in the temperature range 1 MK $< T <$ 30 MK.

The UK-led EUV Imaging Spectrometer (EIS) will observe the emission lines of highly ionized elements in two carefully chosen wavelength bands so as to measure detailed plasma properties with special emphasis on flow velocities and on non-thermal plasma processes over a wide range of plasma temperatures (0.04 MK, 0.25 MK, 1.0 MK $< T <$ 20 MK). This paper outlines the scientific goals of the EIS and discusses the properties, calibration and performance of the instrument in detail within the context of the overall Hinode mission.

R. Moye
Artep Inc., 2922 Excelsior Spring Ct., Ellicott City, MD 21042, USA

H. Hara · T. Watanabe
National Astronomical Observatory of Japan, Mitaka, Tokyo, 181, Japan

K. Matsuzaki · T. Kosugi
Institute of Space and Astronautical Science, Sagamihara, Kanagawa 229, Japan

V. Hansteen · Ø. Wikstol
Institute of Theoretical Astrophysics, University of Oslo, P.O. Box 1029, Blindern, 0315, Oslo, Norway

2. Scientific Aims

The scientific aims of the Hinode mission are focused on three main goals:

– Determine the mechanisms responsible for heating the corona in active regions and the quiet Sun.
– Establish the mechanisms that cause transient phenomena, *e.g.*, flares, CMEs.
– Investigate processes for energy transfer from photosphere to corona.

The instruments have been designed to achieve these goals. Instrument operations and science analysis will concentrate on understanding how changes in the magnetic field impact the solar atmosphere in terms of slow evolutionary behavior, small-scale heating, or through more catastrophic events. In pursuing the mission science goals, recognition of *magnetic reconnection-based* physical processes and their quantitative description will be of considerable importance for understanding the responsive behavior of the solar atmosphere. Another important area is the identification and description of *wave propagation modes* and any related energy dissipation.

The EIS contribution to the mission aims involves the measurement of line intensities, Doppler velocities, line widths, temperatures and densities for the plasma in the Sun's atmosphere. From these measurements, EIS will probe the physical processes that are prevalent on widely different size scales on the Sun. With the availability of suitable multilayer coatings, the design goals of EIS for operation at $\lambda < 300$ Å were to substantially increase the photon throughput and enhance spectral and spatial resolution over previous spectrometers that had operated at these wavelengths. These improvements have led to an instrument that can obtain useful images of an active region (4×8 arc min) at 2 arc sec resolution in around $1-2$ minutes for 12 suitable emission lines. For a flaring active region loop, a 50 Mm section of emitting plasma can be scanned at 2 arc sec resolution in a time of one minute while achieving plasma velocity and line profile width estimates with precisions of ± 5 km s^{-1} and ± 25 km s^{-1} respectively. A selection from the many topics that will be pursued with EIS is indicated below:

Coronal/Photospheric velocity field comparison in active regions: On active region (AR) spatial scales, the visible filter images from the solar optical telescope (SOT) will provide detailed information on photospheric velocities and their time variation. Both vector and line-of-sight magnetograms will also be available. The detailed observation of related intensity, velocity and magnetic configuration changes in the coronal active region plasma has not previously been possible and will be undertaken with EIS observations of loops and other AR magnetic structures.

Coronal AR heating: dynamic phenomena in loops: The understanding of this topic remains elusive. There is evidence for reconnection in loops (*e.g.* Harra, Mandrini, and Matthews, 2004). Much time will be devoted to the detection and characterization of small brightenings by both the EIS and the XRT. EIS in particular will observe any changes in temperature, density and velocity that occur as a result of small events and will obtain evidence of related plasma flows. In addition, the spatially resolved loop temperature and density measurements that EIS will obtain will allow comparison with the output of increasingly sophisticated MHD models (Klimchuk, 2006).

Evolution of trans-equatorial loops: These structures have by definition a significant role for the understanding of large-scale coronal activity. While they appear to participate in large-scale reconnection (Tsuneta, 1996), many of their properties are similar to those of the

smaller loops found in active regions (Pevtsov, 2000). Following their recognition in full-Sun XRT images, EIS will study their foot points in an effort to understand their energetics in relation to the underlying magnetic field.

Coronal seismology: waves in AR structures: Waves are observed on all size and time scales on the Sun—from the 5 minute oscillations in the chromosphere to the large-scale shock waves related to flares and coronal mass ejections. They may have a key role in the supply of the energy to the corona and have been demonstrated to exist in coronal structures (*e.g.*, Williams *et al.*, 2002). It is also clear that their detection and mode identification will allow the measurement of important coronal parameters, *e.g.*, magnetic field (Nakariakov and Ofman, 2001). Spectroscopic observations of oscillations in coronal loops have been made in flaring and post flare conditions (Wang *et al.*, 2002, 2003), while on a larger scale spectroscopic observations of EIT waves in the corona have been pioneered by Harra and Sterling (2003). Progress in these important areas requires observations at the better cadence that EIS will provide.

CME onsets and signatures: CMEs almost certainly involve reconnection. Magnetic breakout scenarios (*e.g.*, Antiochos, DeVore, and Klimchuk, 1999), require the removal of overlying magnetic field structures. In the case of eruption of twisted flux ropes (Williams *et al.*, 2005), this removal process permits an eruption that is driven by the energy stored in the twisted field. So far, CMEs have largely been studied with limb observations by coronagraphs. Velocity measurements by EIS will allow the early stages of the field removal to be identified on the disc and the degree of twist in the erupting material to be assessed. Current CME models predict different plasma dynamic signatures. Here again, EIS velocity measurements will have a key role in testing model validities.

Flare produced plasma: source, location and triggering: The production of high temperature plasma in the corona following solar flares continues to be controversial. Bragg spectrometer observations of flare plasma with good spectral resolution by the Yohkoh BCS (Culhane *et al.*, 1991) have had poor spatial resolution. However Warren and Doschek (2005) have reported a hydrodynamic model that involves energy release in successive sub-resolution threads within loops and appears consistent with the plasma velocities observed by the Yohkoh BCS. EIS will image flare lines from *e.g.* Fe XXIV, with good spatial and temporal resolution which, together with XRT context observations, should clarify the plasma production questions.

Flare reconnection: inflow and outflow: While there has been a lot of observational evidence for reconnection in flares (*e.g.*, Masuda *et al.*, 1994; Tsuneta, 1995), there remain inconsistencies in detail. In particular, spectroscopic data are lacking on outflow and inflow velocities. Much evidence for reconnection has been based on imaging alone (*e.g.*, Yokoyama *et al.*, 2001). We require spectral images with high temporal resolution in the corona. EIS is designed to address this difficult problem.

Quiet Sun transient events: network, network boundaries, Coronal Hole boundaries: Evidence has also been found for reconnection in the quiet Sun, around convective cell boundaries (*e.g.*, Innes *et al.*, 1997) and at coronal hole boundaries (*e.g.*, Madjarska, Doyle, and van Driel-Gesztelyi, 2004), resulting in bi-directional jets. Heating has been observed at the cell boundaries (*e.g.*, Harrison, 1997) and even within the cells themselves (Harra, Gallagher, and Phillips, 2000). There is some dispute as to the cause of the bi-directional jets (often termed explosive events) and of the events that are registered through heating or density change (often referred to as blinkers). EIS will enable us to distinguish between these and determine whether they are indeed different phenomena.

The coronal emission lines registered in the two EUV pass bands of the EIS instrument along with the magnetic field data provided by the SOT and the structural context information from the XRT, will allow significant advances to be achieved in the above areas and in many other facets of solar coronal physics.

3. Instrument Overview

Previous spectrometers designed to operate in orbit in the 50 to 500 Å wavelength range have employed grazing incidence optical systems (mirrors and diffraction gratings) since the normal incidence reflectivity at these wavelengths is vanishingly small for the usual optical materials (*e.g.*, SOHO CDS; Harrison *et al.*, 1995). In addition, the microchannel plate array detectors commonly used, although providing good spatial resolution, exhibited quantum efficiencies (QE) $\leq 20\%$ and required hygroscopic coatings, *e.g.*, KBr. Uncoated microchannel plates have substantially lower QE values. The design of the EIS instrument allows normal incidence operation of the optical elements through the use of multilayer coatings applied to both mirror and grating. In addition, the use of thinned back-illuminated CCDs to register the diffracted photons allows QE values to be achieved that are two to three times greater than for microchannel plate systems. A disadvantage stems from the comparatively narrow passband achievable with an individual multilayer. At the time the instrument was designed, the wavelength range obtainable from available multilayers was 80 Å $< \lambda < 350$ Å. However, enhanced knowledge of the coronal emission line spectrum means that these limitations can be tolerated in the interest of achieving high throughput.

The optical design and layout of the instrument are shown in Figure 1. The spectrometer has a large effective area in two EUV spectral bands through the use of Mo/Si multilayer coatings optimized for high reflectivity in the ranges $170-210$ Å and $250-290$ Å. Solar radiation enters through a thin 1500 Å Al filter which stops the transmission of visible radiation. Photons are focused by the primary mirror onto a slit and are then incident on a toroidal concave grating. Two differently optimized Mo/Si multilayer coatings are applied to matching halves of both mirror and grating.
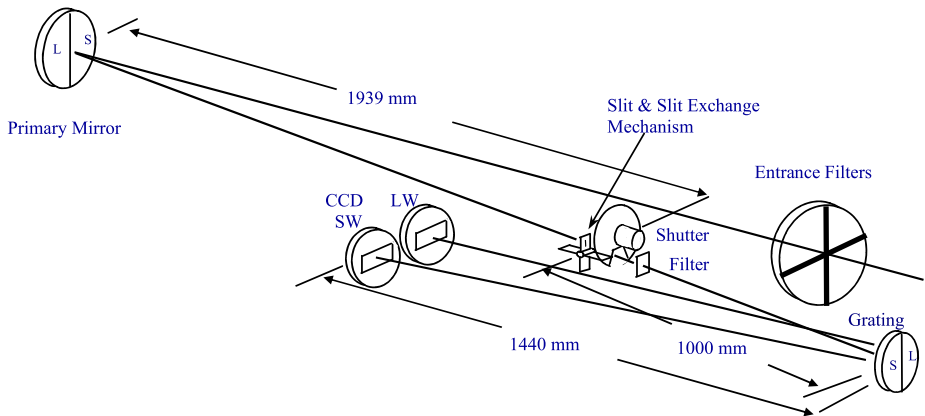

Figure 1 Optical layout of the spectrometer. Components are labeled and dimensions are given in mm. S/SW and L/LW refer to short and long wavelength bands.

Table 1 EIS performance parameters.

Wavelength bands	170 – 210 Å and 250 – 290 Å
Peak effective areas[a]	0.30 cm^2 and 0.11 cm^2
Primary mirror	15 cm diameter; two Mo/Si multilayer coatings
Grating	Toroidal/laminar, 4200 lines/mm, two Mo/Si multilayers
CCD cameras	Two back-thinned e2v CCDs, $2048 \times 1024 \times 13.5$ μm pixels
Plate scales[a]	13.53 μm/arc sec (at CCD); 9.40 μm/arc sec (at slit)
Spatial resolution (pixel)	2 arc sec (1 arc sec)
Field of view	6 arc min $\times$ 8.5 arc min, offset center: ±15 arc min E-W
Raster	1 arc sec in 0.7s[b] (Minimum step size: 0.123 arc sec)
Slit/slot widths[a]	1, 2, 40 and 266 arc sec
Spectral resolution[a]	47 mÅ (FWHM) at 185 Å; 1 pixel = 22 mÅ or approx. 25 km s^{-1} pixel^{-1}
Temperature coverage	Log T = 4.7, 5.6[c], 5.8[c], 5.9[c], 6.0 – 7.3 K
CCD frame read time	0.8 s
Line observations	Simultaneous observation of up to 25 lines

[a]Measured values.

[b]Raster steps occur during CCD readout sequences.

[c]Quiet Sun lines of Fe VIII, Si VII, Si VIII; count rates $\approx 0.5 – 1.0$ counts s^{-1} pixel^{-1}.

Diffracted radiation is registered by a pair of thinned back-illuminated CCDs. Exposure times are controlled by a rotating shutter while a slit exchange mechanism can allow selection of four possible apertures — two spectral slits and two spectral imaging slots. A second thin Al filter is mounted behind the slit/slot mechanism to provide redundancy. The larger entrance filter is housed in an evacuated enclosure that will give protection from acoustic stress and debris during the launch. Raster scanning capability is provided by a piezoelectric drive system which rotates the primary mirror. The raster scan range of 6 arc min in the dispersion direction and the useable slit height of 8.5 arc min set the overall instrument field of view. In addition, there is a coarse mechanism that can offset the mirror by ±15 arc min from the spacecraft pointing axis in an E-W direction. The grating has a focusing mechanism for on-orbit adjustment. The instrument properties are summarized in Table 1.

All of the components shown in Figure 1 are mounted in a composite structure which, because of its low Coefficient of Thermal Expansion (CTE), acts as a stable bench for the optical components. A cooling radiator on the outside of the structure maintains the CCDs at $<-50°$C at expected operating conditions. With the front filter enclosure doors closed, the interior of the spectrometer can sustain a slight positive pressure when under dry nitrogen purge. The latter is maintained throughout the period when the instrument is on the ground and is only to be removed about two hours before launch when the spacecraft is inside the fairing of the third stage.

An electronic overview of the EIS instrument is given in Figure 2. The primary digital and power interfaces between EIS and the spacecraft are handled by the Instrument Control Unit (ICU). There are three digital interfaces, command, housekeeping (status) and science (mission data). All three have serial differential format. The ICU hosts compiled C software running on a TEMIC 21020 Digital Signal Processor (DSP) that interprets commands and controls the instrument engineering and science operations. The software gathers housekeeping and returns it to the spacecraft, monitoring the health of selected parameters and
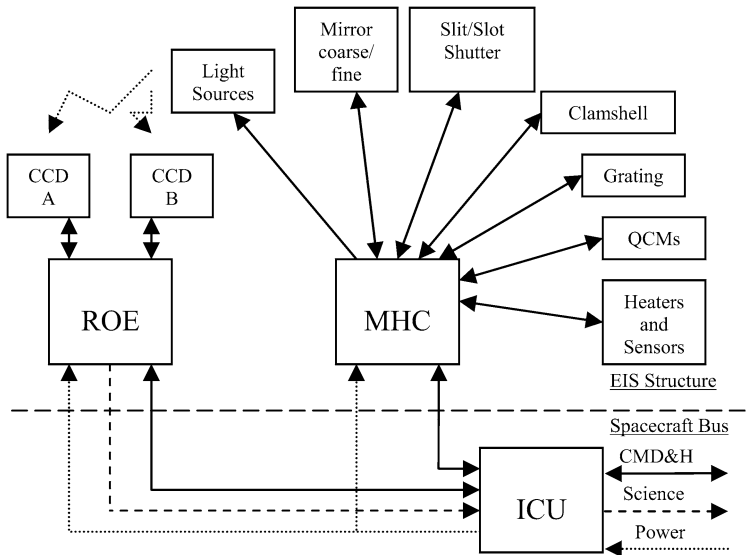
Figure 2 EIS electronic diagram showing the instrument subsystem interconnections.

putting the instrument into a safe mode should any exceed defined limits. The software also packetizes science data and sends them to the spacecraft via the science interface.

The power interface is a 28 V regulated bus. The ICU contains a DC/DC converter which supplies isolated secondaries for the ICU and the camera Read Out Electronics (ROE). No switching power conversion is done in the ROE to minimize local noise generation. The 28 V power for the Mechanism and Heater Control (MHC) unit is controlled by switches in the ICU. The MHC houses its own power converters.

Digital communication for commanding and housekeeping between units within the instrument is facilitated by separate RS422 interfaces between the ICU and ROE and between ICU and MHC. For the science data there is a dedicated 32 Mbps link from the ROE to the ICU. The ROE interfaces to the CCDs and the MHC interfaces to the EIS structure mechanisms, quartz crystal microbalances (QCMs), CCD light sources, heaters and temperature sensors. Heaters to replace the heat dissipated by the ROE and MHC when they are off (make-up heaters) along with CCD bake-out heaters and temperature sensors for decontamination of the CCDs are operated by the ICU. In addition to the above ICU interfaces, there are direct connections from the spacecraft to the spectrometer structure for temperature sensors and survival heater circuits.

The EIS grounding scheme is chosen to give the best ROE noise performance. There is a single point ground for the EIS ICU and ROE secondary power which is at the ROE. There is also a single point ground for the MHC power systems via a link at the spectrometer Connector Panel (CNP). The ICU/ROE and MHC grounds are joined together at the CNP which is then connected to the spacecraft ground. The composite structure resistance is not low enough to guarantee a Faraday cage effect so the spectrometer harness is screened. The electrically conducting Multi-Layer Insulation (MLI) external to the structure also helps to screen the internal electronics.

The CCD camera electronics and the MHC unit are located within the spectrometer section. The independent EIS ICU and the spacecraft Mission Data Processor (MDP) are

located in the spacecraft service or bus section at ≈2.5 m from the spectrometer. Observation tables, loaded in the EIS ICU from the MDP, organize the readout of data from the CCD cameras with a maximum of 25 user-selected spectral windows being allowed by the software. The ICU also generates commands for operating the scanning, shutter, and slit interchange mechanisms to execute appropriate sets of observing sequences or studies. The spacecraft mass memory has a total capacity of 7 Gbits for the instruments and the nominal EIS share of this is 15%. Thus instrument data throughput is set by the number of ground station contacts per day. Provision of access to the Norwegian Svalbard ground station by ESA and the Norwegian Space Agency will allow at least 15 ground station contacts each day in addition to the four daily contacts with the JAXA station at the Uchinoura Space Centre (USC). Thus EIS, using lossless data compression, will be able to operate at a data rate of ≈100 kb/s.

Following the SOHO CDS instrument, EIS will provide the next steps in EUV spectral imaging of the solar corona and upper transition region. It will have approximately a factor of ten enhancement in effective area due to the use of multilayer coated optics and back-illuminated CCDs. Spectral resolution is also improved by a factor of ten in the wavelength ranges being observed. While at 2 arc sec, the spatial resolution is a factor two to three better than that of CDS.

4. Optical Design and Instrument Components

An optical schematic of EIS which gives the locations of the components is shown in Figure 1 and has been briefly discussed in the previous section. A detailed account of the instrument's optics and mechanisms is given by Korendyke *et al.* (2006). The telescope primary mirror images EUV radiation from the Sun onto the spectrograph slit. Light passing through the slit is dispersed and stigmatically re-imaged by the toroidal grating onto two 1024×2048 pixel CCD detectors, each with 2048 pixels in the dispersion direction. In flight, the mirror can be rotated in ≈0.125 arc sec steps about the Y axis (solar N-S) to sample different solar structures with the slit. High-resolution spectroheliograms (raster images) are formed by steadily moving the solar image in fine increments on the spectrograph slit and taking repeated exposures. An interchange mechanism allows selection among two slits (1 and 2 arc sec width) and two slots (40 and 266 arc sec width). The slot observations of the solar disk obtain images of large areas in bright solar emission lines with a single exposure. For the 40 arc sec slot, spectrally pure images are available for several strong lines in each passband. The slot images exhibit a modest spatial blur along the dispersion direction.

Both mirror and grating operate at near normal incidence. To broaden the spectral range, the multilayer-coated optical elements were divided into two D-shaped sectors; each sector was coated with a multilayer tuned to produce high reflectivity in its wavelength band. These coatings achieved peak reflectivities of 32% and 23% in the $170 – 210$ Å and $250 – 290$ Å bands, respectively. Optimum response is achieved for each band by careful selection of thickness for the individual Si and Mo layers (Seely *et al.*, 2004). The telescope mirror is a superpolished off-axis parabola with a focal length of 1939 mm, a measured figure accuracy $<\lambda/47$ rms at 6328 Å and a microroughness of <4 Å rms. The 160 mm diameter mirror was fabricated from Zerodur by Tinsley Laboratories, Inc. and has a usable diameter of 150 mm. The flight grating is specified to be a toroid (Beutler, 1945; Haber, 1950) with radii of 1182.98 mm in the dispersion direction and 1178.28 mm in the perpendicular direction with a figure slope error <0.5 arc sec RMS. The grating microroughness is <2.5 Å RMS. The gratings were fabricated by Carl Zeiss Laser Optics GmbH from 100 mm diameter fused silica blanks and have a usable area of 90 mm diameter.

4.1. Entrance Filter and Housing

In the 1970s, NRL in collaboration with G. Steele of Luxel Corp. developed large format thin aluminum filters for the EUV instruments on Skylab (Schumacher and Hunter, 1977). High purity vapor deposited aluminum (VDA) foils between 1000 Å and 1500 Å thick pass EUV wavelengths between 170 Å and 650 Å while blocking visible, infrared and near UV wavelengths (Powell, 1992). We have implemented a set of four Al filters of this type for the EIS front aperture and a second smaller Al filter behind the spectrometer slit to reject out of band light that might leak through pinholes. For the launch, the thin foils of the entrance filter must be protected from severe vibration, the acoustic and debris environment, and from oxidation and contamination. A special chamber was built for launching the filters under vacuum (Figure 3). It is a short cylinder having front and rear doors hinged to open in the vacuum of space much like a clam and is thus named the Clamshell (CLM) assembly. In orbit, the doors are opened by high output paraffin (HOP) thermal actuators.

The CLM and filter arrangement evolved from similar units used on the TRACE mission (P. Cheimets, 1999, private communication), with the front aperture divided into four quadrants, each with its own filter (Figure 4). The thin Al filters are supported on a nickel mesh of 40 μm wires on 390 μm centers. Each mesh has an open area equal to 80% of the total. Meshes with attached foils were glued to Al frames for installation. Each frame has a blackened tongue and groove air passage around its margin to allow air pressure to equalize on the two sides of the filter.

The EUV transmission of each filter was measured with synchrotron radiation at the X24C beamline of the National Synchrotron Light Source (NSLS) at the Brookhaven National Laboratory. The synchrotron beam passed through a monochromator and sampled an ≈2 mm diameter spot on the filter. Each filter was measured at a grid of points on 15 mm spacing. Figure 5 shows a summary plot of the transmission of a typical filter, in this case
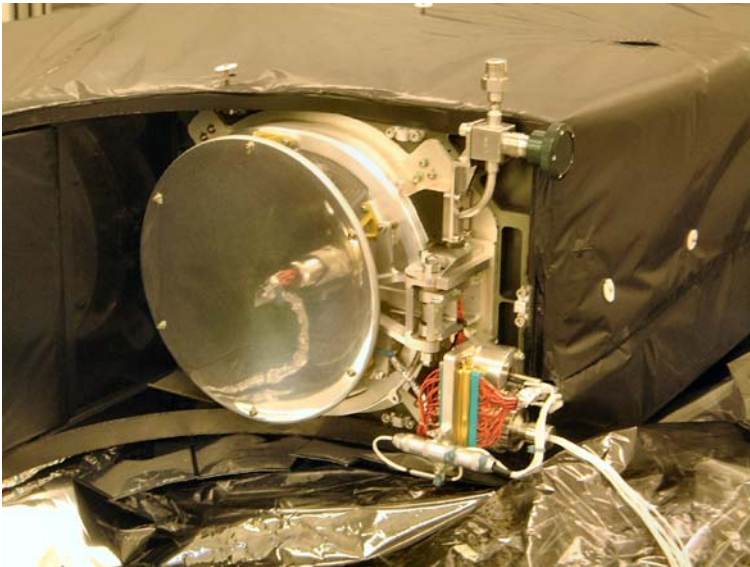

Figure 3 EIS Clamshell assembly mounted on instrument. The evacuation port is at the top and a thin polished metal sun shield disk on the front reflects incoming solar radiation. The instrument itself is covered with black thermal blanketing material.

Figure 4 Engineering model of EIS front filter array. Four frames are in place. This view of the array is before the aluminum foils were mounted.

Figure 5 Average transmission for a 1500 Å Al filter. The data are from 24 scans at points on a 15 mm grid arranged over the filter surface. The error bars are $\pm 1\sigma$. These data are for the mounted filters and include the $\approx 15\%$ loss due to the mesh. The step at 170 Å is due to the Al absorption L-edge.
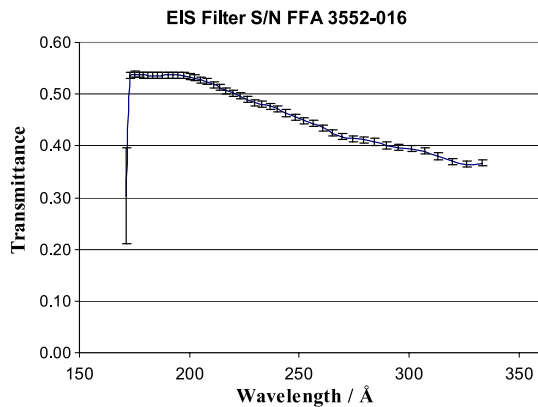
1500 Å thick. Another filter property measured was the visible light rejection. The visible transmission fraction was $\leq 8.3 \times 10^{-7}$ for all filters.

4.2. Primary Mirror and Scanning Mechanisms

The articulated primary mirror produces a high quality solar image at the spectrograph entrance slit. The mirror mechanism provides two different types of articulation for moving the solar image perpendicular to the slit. A piezoelectric transducer (PZT) actuator and flex-pivot arrangement provides a tilt motion about a N-S line through the mirror center. The maximum mirror tilt is 300 arc sec and the image motion at the slit is therefore 600 arc sec. The measured reproducibility of the mirror movements was better than 2 arc sec over about 30 minutes time in a laboratory environment. Nominal rastering operations will be conducted by tilting the mirror in fine increments with the PZT. This produces an E-W motion of the solar image through a small range. Linear mirror motion is provided by a ball screw

Table 2 Predicted EIS mirror imaging performance.

Contributing error	Applicable tolerance	Spot diameter [μm]	Comments
Optical aberrations	<150 μm along axis	<13.5	Modeled geometric and diffraction effects
PZT electrical noise		<7.75	Measured
Focus error budget		<11.1	Sensitivity of focus test
Total		19.12	Root sum square

Note: Equivalent spot diameters are for CCD focal plane. Diameters twice rms radii.

and linear bearing arrangement. The step size is equivalent to 0.30 arc sec on the solar surface with a total range greater than ±2750 steps or ±825 arc sec. Linear mirror travel is perpendicular to the chief ray from the mirror center to the slit center. In orbit, the linear motion will be used to re-point the instrument field of view. It also moves the solar image in the E-W direction on the slit, but the range is larger than that of the PZT tilt. The linear motion of this mechanism may disturb the fine pointing of the Solar B spacecraft and hence its operation is restricted. However, the EIS instrument can use this mechanism to observe emerging activity at the limbs on occasions when the SOT may be studying mature active regions at disc center.

The predicted image quality of the mirror is shown in Table 2. The ray trace spot diameters degrade slowly as a function of field angle and mirror position. For a nominal raster using the PZT with a field of view of ±250 arc sec along the slit and a total raster width of ±250 arc sec, the rms spot diameter is 0.8 arc sec at the corners. A linear excursion of the primary mirror of 900 arc sec results in a ray trace spot diameter of 1.9 arc sec at the center of the slit. During normal operations, the maximum expected repointing adjustment is <2 arc min with spot diameters <0.3 arc sec. Overall, the expected ray trace/geometric spot diameter is <0.7 arc sec within a field of 250 arc sec radius. The EIS primary mirror with a λ/47 rms reflected wavefront error operated at EUV wavelengths will achieve ≈0.6 arc sec diameter diffraction limited performance. A more complete discussion of diffraction theory of aberrations is given in Born and Wolf (1964). With equivalent diffraction spot diameter of ≈0.6 arc seconds and expected ray trace spot diameters of <0.7 arc sec, we expect to achieve <1 arc sec spot diameters from the mirror optic. The rms microroughness (<0.3 nm) is sufficient to obtain high quality EUV imaging. Typical large telescope microroughness in the visible is 2 nm rms, which is comparable to the scaled situation in EIS. The wings and overall shape of the point spread function at the slit should be similar to that of present orbiting telescopes (TRACE and EIT/SOHO) with prefilters. The telescope imaging was verified to be <2 arc sec in the flight configuration. We illuminated the front aperture with visible light using a high quality collimator and examined the resulting image at the slit plane with a microscope arrangement. We were able to clearly discern <2 arc sec resolution on the projected and subsequently re-imaged 1951 USAF resolution target. A similar optical setup was used to focus the telescope.

The components of the mirror mechanism are shown in Figure 6. The central hub is bonded to a bracket with flexible epoxy. The bracket is mounted on two flexible pivots and attached to the linear moving stage of the mechanism. The PZT actuator provides the rotary (mirror tilt) motion. Strain gauges in the PZT sense the extension and remove hysteresis. Open and closed loop PZT performance is shown in Figure 7. The linear moving stage
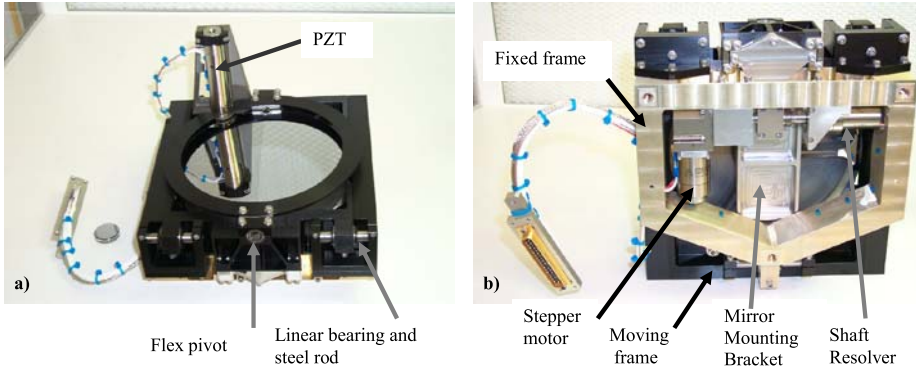
Figure 6 The assembled flight mirror subsystem (a) front view and (b) rear view.
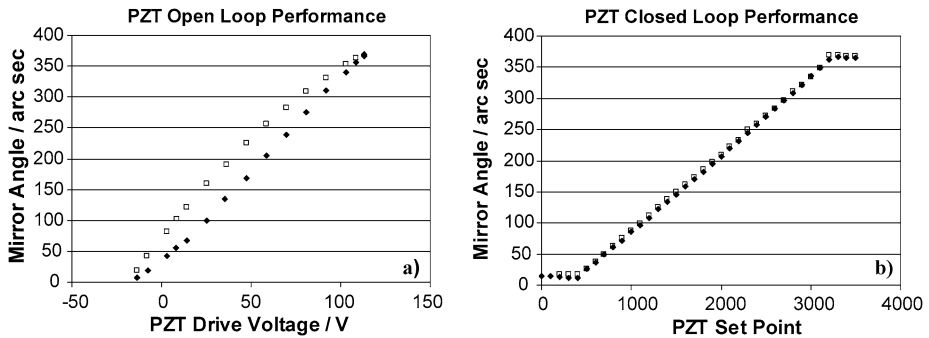

Figure 7 Open (a) and closed loop (b) PZT performance. Rotation angle plotted as a function of control loop set point and as a function of PZT voltage. Solid diamonds are for increasing PZT voltage and open squares are for decreasing PZT voltage. The useful PZT set point range is between 600 and 3200.

is attached to a fixed frame with three linear, self-aligning bearings mounted on hardened steel shafts. A linear actuator, attached to the fixed frame, consists of a 30 degree stepper motor with a gearbox and ball screw. It drives a ball nut attached to the moving frame. The residual displacement errors are periodic in nature with maximum amplitude of ± 15 μm or 1.6 arc sec on the solar surface.

4.3. Shutter and Slit Exchange Mechanisms

The EIS instrument incorporates a slit/slot interchange mechanism shown in Figure 8a. This mechanism enables selection of one of four instrument slits/slots to support various observation programs. Each slit and its aluminum frame are bolted to a paddle wheel. Tight fabrication tolerances on the frame and paddle wheel control the placement of the slits. The paddle wheel (Figure 8b) is directly attached to the output shaft of a rotary actuator whose axis of rotation is perpendicular to the chief optical ray. The rotary actuator reproducibly places each of the spectrometer slits in the telescope focal plane. A geared rotary resolver is attached to the output shaft of the stepper motor and has an accuracy of better than 15 arc min, sufficient to discriminate between individual motor steps. The instrument slits and slots were fabricated by etching from a silicon substrate. Precise metrology was carried out to determine the slit width, results of which are shown in Table 3.

Figure 8 (a) Slit/slot
mechanism assembly. The four
slits are on a paddle wheel and
are exchanged by 90 degree
rotations of the wheel. The
shutter blade and motor are also
attached to this assembly.
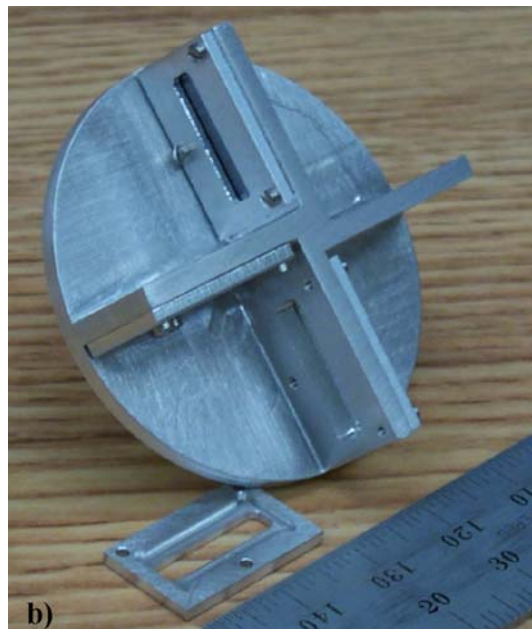(b) Paddle wheel and slit frame
before blackening.

Table 3 EIS slit width summary.

Nominal width [arc sec]	Serial number	Measured width [μm]	Measured width [arc sec]
1	101C	9.5	1.01
2	102A	19.0	2.02
40	103A	384	40.9
266	104D	2506	266.6

Note: Measured accuracies are ±0.5 μm for the 1 and 2 arc sec slits and ±2 μm for the 40 and 266 arc sec slots.

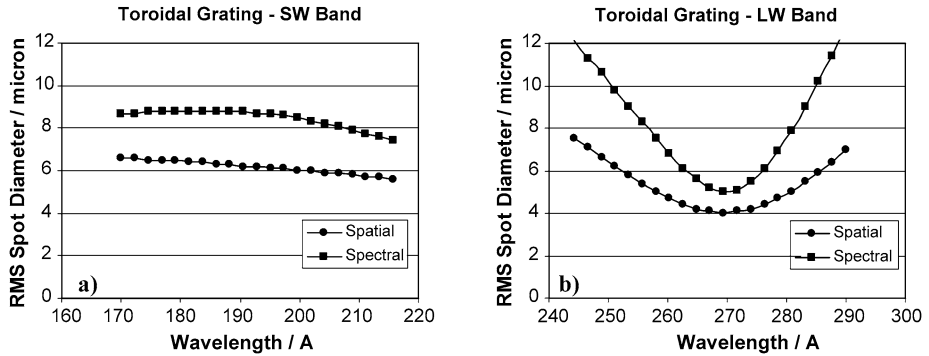**Figure 9** Grating spot size diameter for a point at the center of the slit as $f(\lambda)$ for (a) short wavelength band and (b) long wavelength band.

As shown in Figure 8a, the shutter assembly is combined with the slit interchange assembly. During laboratory testing, the shutter and associated flight drive electronics successfully obtained a series of 100 ms exposures with <5% photometric error. The shutter motor is a brushless DC unit available from Kollmorgen. The necessary commutation is provided by an optical encoder assembly mounted to the shaft of the motor. The motor was specifically designed to provide the high speed and high torque for precise control of rotating assemblies required by this application.

4.4. Concave Grating

The grating mount geometry was optimized using a ray tracing program. The grating ruling frequency was chosen to be 4200 lines/mm, being the limit of the holographic recording equipment at the time of fabrication. The general constraints included an overall instrument length of ≈3 m, a required plate scale of 1 arc sec/pixel, and 13.5 μm CCD pixels. Within these limitations, a ray tracing code optimized the grating parameters to provide the smallest averaged RMS spot size over the spectral bands 170–210 Å and 250–290 Å and over a spatial field of view of ±250 arc sec. The optimization calculation used separate D-shaped portions of the grating for each wavelength range but was constrained to use an identically figured and singly ruled grating for the entire EIS range. This optimization step resulted in a different optical prescription and smaller spot sizes when compared to gratings optimized using the full grating aperture for both wavelength ranges. Representative plots of the rms spot diameters against wavelength and field angle along the slit are given in Figures 9 and 10. Performance as characterized in the laboratory closely approaches these theoretical values. The predicted grating imaging performance is included in Table 2.
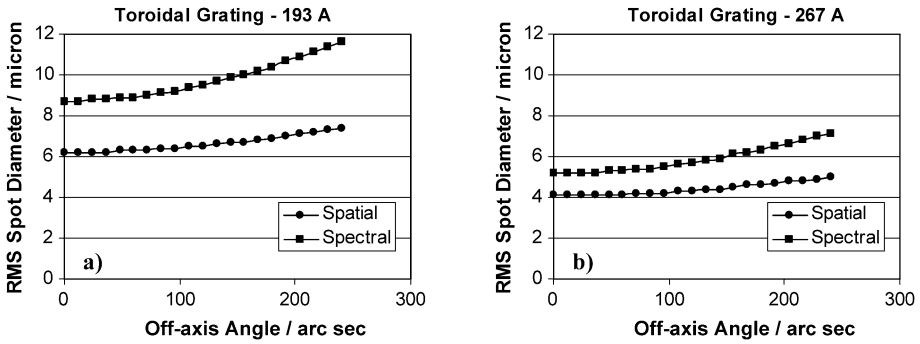
Toroidal Grating - 193 A

Toroidal Grating - 267 A

Figure 10 Grating spot size diameter along the slit at the central wavelength of each detector. (a) for the short wave band and (b) for the long wave band. Position 0 is slit center and the off-axis angle is measured North or South along the slit.

Figure 11 AFM profile of grating grooves in a 1 μm×1 μm region for a typical EIS grating. The mean groove depth in this case is 64 Å and the land width is 1080 Å.
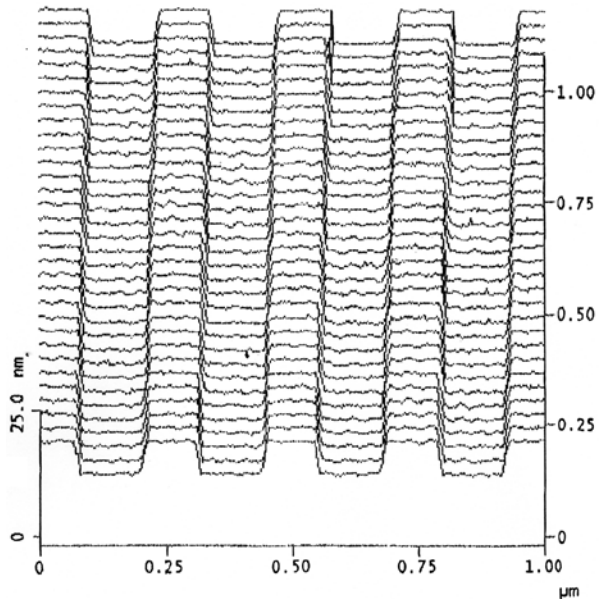
The grating pattern was holographically recorded and subsequently ion etched into the fused silica blank. A single uniform laminar line pattern, with a frequency of 4200 lines/mm, groove depth of 60 Å, and land to groove ratio of 0.85:1 was chosen to provide nearly equal diffraction efficiencies in the two EIS spectral bands. This grating configuration illuminated at near normal incidence should maximize the diffraction efficiency in the first order, while minimizing the efficiencies in other orders (Seely *et al.*, 2004; Kowalski *et al.*, 1999). Figure 11 shows the results of an Atomic Force Microscope (AFM) measurement of the groove profile of an EIS laminar grating. The multi-layer coated grating efficiencies for the zero and first orders are shown in Figure 12. The peak first order efficiencies are 8.0 % at 196 Å in the short wavelength band and 7.9 % at 271 Å in the long-wavelength band.
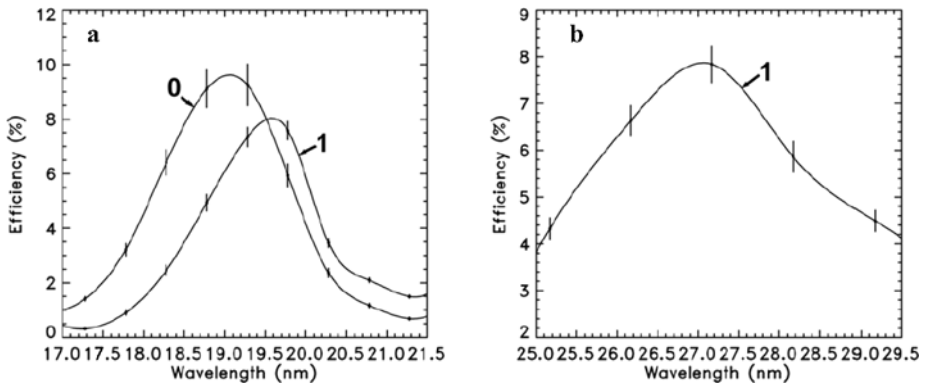
Figure 12 Grating efficiency in the short (a) and long (b) wavelength bands. Grating order number (m) is indicated. For m greater than $2-5$, the measured grating efficiency is $<1\%$.

Figure 13 Grating FL-7 in its flight mounting. Two of the four alignment facets on the margin of the grating blank are visible. The focus mechanism includes motor, gearhead, and ball screw. Two small circuit boards hold LEDs and photodiodes for the limit sensors.

The EIS grating mounted in its focusing mechanism is shown in Figure 13. The rear surface of the grating is bonded to a mounting bracket at the grating center with the same flexible epoxy used for bonding the mirror. The grating and bracket subassembly are attached to a moving stage mounted to the mechanism base plate with a pair of crossed roller bearing slides. The moving stage is driven by a geared stepper motor and ball screw combination. Each motor step results in a 2.8 μm displacement of the grating. The mechanism is aligned to drive the translation stage along the slit-grating axis.

4.5. Dual CCD Camera and Readout Electronics

The EIS camera consists of the Read-Out Electronics (ROE) unit and two CCDs, on a Focal Plane Assembly (FPA), at the focus of the spectrometer. Two CCDs are required to cover

both the short (170 to 210 Å) and long (250 to 290 Å) wavelength ranges. Radiation from the solar region of interest is focused and dispersed by the EIS optics (Figure 1) into these two wavelength ranges and imaged by the two CCDs.

The EIS CCDs are type CCD 42-20, made by e2v Technologies. They are back-illuminated and thinned to maximize the quantum efficiency. There are 2048 imaging pixels in the dispersion direction and 1024 pixels in the spatial direction. They are three-phase devices which operate in full-frame mode with readout ports at both ends of the readout registers. Pixel size is 13.5 μm × 13.5 μm, which is equivalent to 1 arc sec in the spatial dimension and 0.0223 Å in the spectral dimension. The CCDs are made for Advanced Inverted Mode Operation (AIMO) which allows low dark current levels to be achieved without excessive cooling. For EIS the requirement is $-40\,°C$ and an operational temperature of $<-45\,°C$ is predicted from modeling for all operational conditions. A single dump gate allows the CCD to be rapidly flushed while clocking the CCD vertically. The relatively high electrical capacitance to substrate of the vertical electrodes places a limitation on the rate that the vertical electrodes may be clocked (8 μs/row). However, it is the horizontal readout rate (2 μs/pixel) which dominates the overall readout duration rather than the vertical clock rate. The CCD type 42-20 has 50 overscan pixels at each end of its readout register. On-chip horizontal binning is achieved with a summing well electrode at each end.

The CCD mounting is shown in Figure 14a. Devices are mounted on INVAR plates which have a low CTE of $(1.3 \times 10^{-6}\,°C^{-1})$ which is reasonably matched to that of the silicon imaging surface $(2.6 \times 10^{-6}\,°C^{-1})$. The INVAR plates are mounted on titanium barrels which are attached to the main camera bracket. A Vespel spacer is located between the titanium barrel and the structure to thermally isolate the CCDs. The INVAR plates also support the associated thermal sensor and survival and bake-out heaters. The devices are connected to the ROE by flexible cables and micro-D connectors. The CCD parameters are summarized in Table 4.

For the EIS camera, having ports at each end of the readout registers not only speeds up the overall readout time but also allows for some redundancy so that if one port fails, the ROE can be programmed to read out pixel data from the remaining functional port. Thus
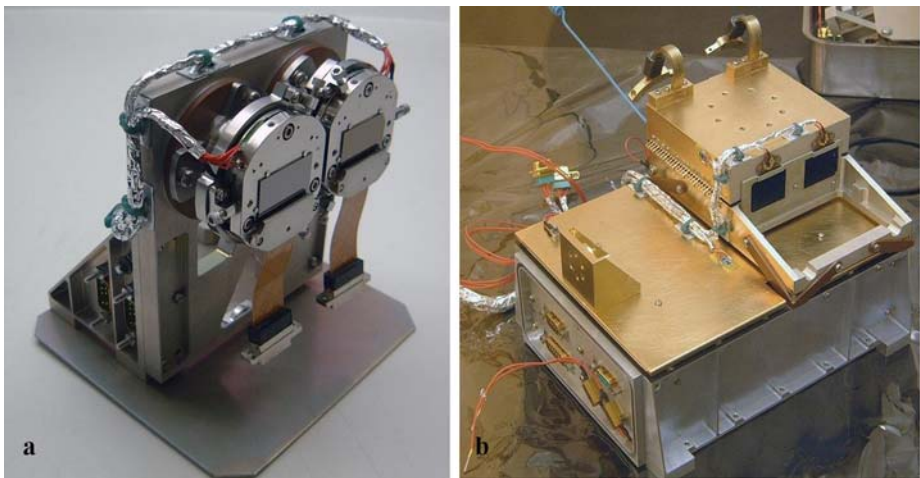

Figure 14 The EIS dual CCD system with (a) the CCDs mounted showing their flexible electrical connections, and (b) the flight readout electronics unit. Cooling strap connections to the CCDs are shown attached to the particle/radiation shield on top of the ROE box.

Table 4 Summary of CCD parameters.

Wavelength range	CCD A	CCD B
	250 – 290 Å	170 – 210 Å
Device type	CCD 42-20	
Array size	2048 × 1024	
Pixel size	13.5 μm × 13.5 μm	
Readout rate	2 μs/pixel	
Full well capacity	90k electrons	
Charge transfer efficiency	0.999996	
Quantum efficiency[a]	39 ± 4%	44 ± 4%

[a]See Section 7.2. Full calibration results suggest that ≈60% may be more appropriate.
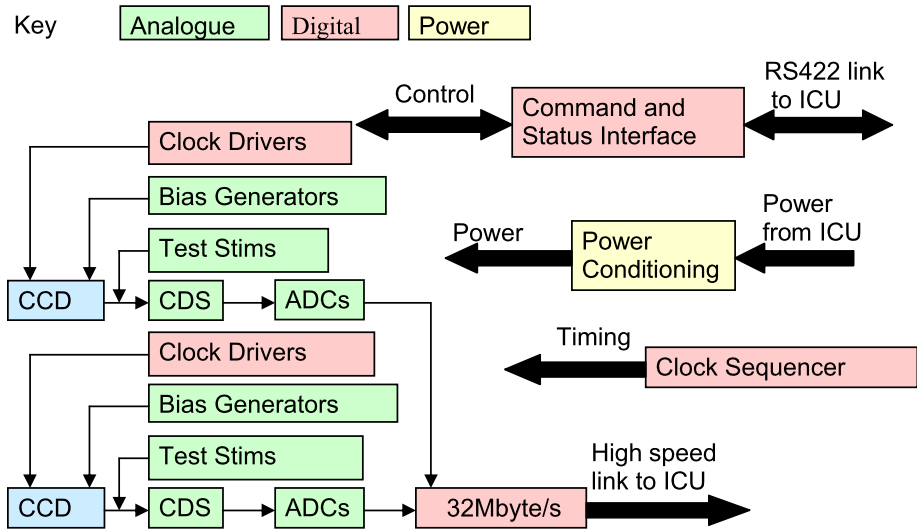

Figure 15 Block schematic diagram of the EIS dual-CCD camera and its readout electronics.

the ROE requires four analog signal chains in order for all four ports to be read out simultaneously. The organization of the camera and readout system is shown as a block diagram in Figure 15. A Correlated Double Sampling technique reduces the CCD reset noise to an acceptable level. Each signal chain produces 14-bit parallel data which a Field Programmable Gate Array (FPGA) combines into a 32 Mbps serial stream. This is transmitted to the EIS Instrument Control Unit (ICU) via a high-speed data link in the telescope harness. The Clock Sequence Generator (CSG) or sequencer is common to both CCDs for simplicity and elimination of cross-talk. There is a local test CSG in the analog electronics for pre-flight testing and noise performance evaluation, and a main CSG in the digital electronics which is programmable from the ICU. The main CSG controls the clocks for the CCD and can also generate stimulation test patterns.

The ROE hardware consists of a motherboard and three daughter boards: power, digital and analog. There are two types of serial link with the ICU. A low-speed (9.6 kbps) bi-directional asynchronous command and status link sends commands to the camera. These include master reset, integration time, CCD window origin and size, and the ports used for read-out. The link receives digitized analog housekeeping and camera status information.

A high-speed link (32 Mbps) using Low Voltage Differential Signaling technology passes the CCD image data to the ICU. The 14-bit data from the four CCD signal chains plus a 2-bit CCD port ID header for each is concatenated into a contiguous 64-bit serial word.

The full well capacity of the CCDs is approximately 90k electrons. With 14-bit Analog to Digital Converters (ADCs), the amplifier gain was set to 6.6 ± 0.03 electrons per Data Number (DN). The full well capacity of the CCD in the long-wavelength range corresponds to ≈ 7500 photons. Due to the photoelectric effect, an incident photon will be converted into a variable number of photoelectrons. At 170 Å, each photon will generate about 20 photo-electrons, while at 290 Å, one photon will generate about 12 photoelectrons. The minimum signal detectable by the CCDs should correspond to one photon which in turn corresponds to 12 photoelectrons at the long-wavelength limit. Thus, the minimum "shot" noise on the detected signal should also correspond to 12 photoelectrons or one photon. To maximize the signal-to-noise ratio, the quantization and read noise values should be below the signal shot noise. Since these terms add in quadrature, there is little advantage in having quantization or read noise values which are substantially below the photon shot noise.

The thermal noise generated at the expected nominal CCD operating temperature of $-50\,°C$ will be minimal (≈ 0.005 electrons pixel^{-1} s^{-1}) except for very long integration times, and will even then still be significantly below the signal shot noise. An amplifier gain of ≈ 6.5 electrons/DN means that the quantization noise is well below the signal shot noise. A readout noise of $\approx 50\%$ of the signal shot noise would correspond to about 6 electrons rms, suggesting a readout time of around 2 µs/pixel.

Subsets of the CCD frames can be selected in hardware for readout. Definable regions on the CCDs are in the form of rectangles selectable up to the full CCD width. Both CCDs must have identical windows which can be up to 1024 pixels wide for two readout nodes or up to 2048 pixels if only one readout node is available. Thus either two or four identical hardware windows can be selected. In the four-window case, pairs of windows must be located symmetrically about column number 1024 on each CCD. The available height is 512 rows. Charge from outside these windows will not be read and can be quickly dumped. A common Clock Sequence Generator leads to the use of identical hardware windows on both CCDs. However, this gives a major benefit of minimizing cross talk on the digitized signal as pixels are clocked out at the same time. Flexible software windows, up to a maximum of 25 in total, can be set to further reduce the pixel data for transmission to the ground. The configuration of these software windows can be independent of CCD and at any location within the frames. Thus particular EUV spectral regions of interest may be selected.

5. Mechanical and Thermal Design

5.1. Mechanical Design

The mechanical design requirements were (a) total structure mass of less than 23 kg set by the capacity of the M-V launcher; (b) high stiffness with a first resonance mode frequency >60 Hz; (c) dimensional stability to maintain spectral and spatial resolution over a broad temperature range and to minimize motion of the spectra on the detectors; and (d) structural three-year condensable molecular fluence of 2.7×10^{-6} g cm^{-2}. This strict fluence requirement restricted the selection of materials within the optics cavity, mandated extensive vacuum conditioning of the EIS structure, and required assembly in a carefully controlled clean environment. The assembled instrument was double bagged and purged during instrument and spacecraft level integration and test.
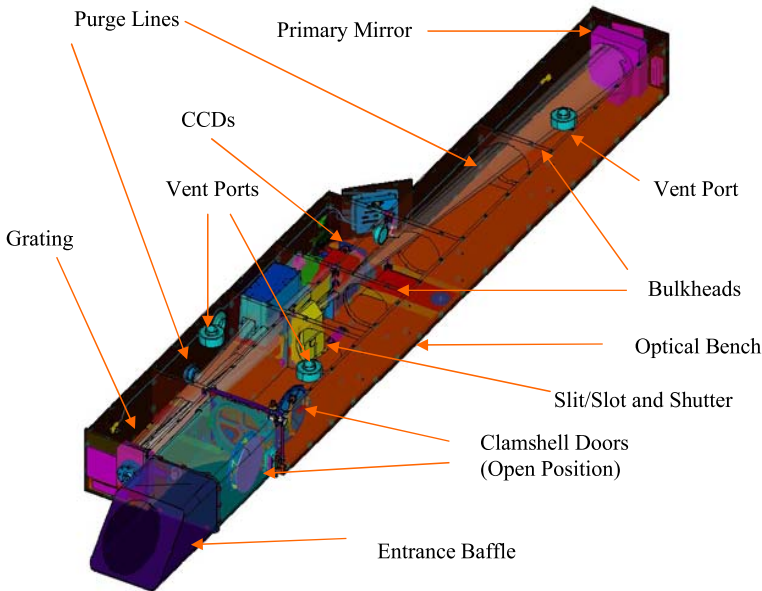
Figure 16 Diagram of the EIS spectrometer structure showing the locations of the principal elements.

The structure chosen used honeycomb sandwich panels with aluminum core material and face sheets made from Carbon Fiber Reinforced Plastic (CFRP). The selected fiber resin combination is M55 with RS3 cyanate ester resin. M55/RS3 has been used extensively in the aerospace industry and shows impressive stiffness to mass ratios with excellent dimensional stability and acceptably low outgassing properties.

The layout of the instrument is shown in Figure 16. EIS measures 3.54 m from the tip of the entrance baffle to the rear bulkhead carrying the mirror. The instrument base panel consists of a 20-mm-thick Al core with nominal 1-mm-thick face sheets and 1-mm reinforcement patches near the instrument interface points. The EIS is mounted on a semi-kinematic titanium suspension between the instrument interface points (titanium inserts) and the central cylinder of the payload module. The width at the widest point of the instrument is 0.55 m and the height is 0.25 m.

The effective CTE of the optical bench was measured using coupon samples and is less than 0.4 ppm/°C. The allowed thermal gradient variation in orbit with this CTE is 10°C. The bulkhead skins consist of balanced quasi-isotropic layers of 0/+60/-60 deg orientation. The instrument sidewalls and bulkheads consist of 10-mm-thick core with 0.6-mm-thick face sheets. The mass of the bare structure totals just below 23 kg which is 40% of the overall instrument mass (including all optical units, electronics boxes, wiring harness and thermal hardware).

The assembly of the instrument's panels was done in stages to ensure proper cleanliness and stress relief before final integration. All panels including the base panel or optical bench were thoroughly cleaned as parts and then "dry" assembled leaving small clearances between the internal bolted faces and edges. All edges were capped with CFRP U-shaped strips to close the vented aluminum honeycomb core. The face sheets facing outwards were all perforated with a rectangular pattern of small holes. This is to ensure that all gas trapped inside the sandwich was vented directly to the outside of the instrument. The Al honeycomb material was also perforated to permit venting of the individual cells.

The dry assembly was thermally cycled in a vacuum chamber to stress-relieve the structure. Following this step, all strength- and stiffness-critical bulkheads were bonded together with strips of L-shaped CFRP. The edges that were prone to rubbing due to mechanical loading were coated with adhesive to seal the fiber particles on the machined edges. The structure was then returned to the bake-out chamber for a six-week vacuum bake-out with constant QCM monitoring, to clear all outgassing species. After verification and confirmation that the structure met the outgassing fluence requirements, the optical components and electronics boxes were mounted. These were all baked out separately prior to final assembly.

Following final integration and alignment verification the instrument was kept purged during all stages, except during mechanical acceptance, thermal balance and thermal vacuum testing. The purge lines are integrated in the structure and inject ultra-clean nitrogen near all optical components (mirror, grating and CCDs). Vent ports located in the lid of the instrument away from these injection points allow rapid evacuation and ensure flow away from the optical surfaces. The instrument entrance is blocked by the clamshell doors sealing the 1500 Å Al filters and keeping them under vacuum.

The locations of the optical paths and components within the structure are shown in Figure 17. After passing the entrance baffle and filter, radiation is incident on the mirror with the light aperture bulkheads being positioned to absorb most of the stray light. The beam then passes through a slot in the central panel and through the slit/slot mechanism. It is then diffracted by the grating while the zero order is absorbed on the bulkhead ahead of the MHC box (blue in Figure 17). The separately diffracted short- and long-wavelength beams pass through a baffle in the particle radiation shield before hitting the surface of the CCDs. Calibration Light Emitting Diode (LED) sources are mounted inside the particle radiation shield.

The outgassing of the CFRP used for the structure was measured by Outgassing Services International. A test sample was subjected to vacuum bake at 80 °C for 72 h and at 40 °C for 67 h. Using a TQCM, outgassing was measured at collection temperatures of 80 K, 213 K, 253 K and 293 K. The 80 K measurement is the reference for all species condensable down to 80 K. The other measurements show negligible outgassing for species of higher molecular weight (see Table 5).

Data for a temperature of 80 °C are given in the table. Extensive outgassing beyond 72 h was required to reach the desired fluence rate in the flight structure. The main outgassing species was water (>99%). Other materials that outgas were used during the manufacture and assembly, *e.g.*, Hysol 9395, Eccobond 285 and Scotch-Weld 1838. Where practical the adhesives were put under vacuum after careful mixing to release all excess gas before application and curing.
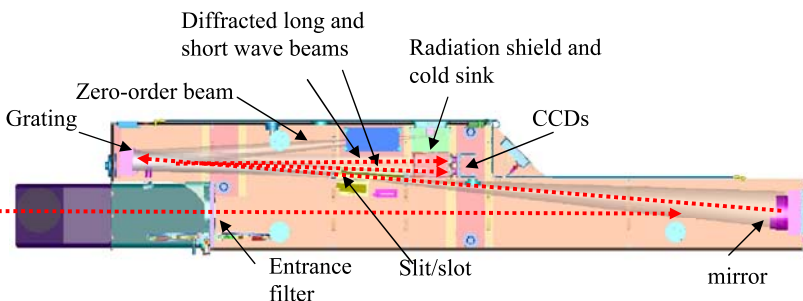

Figure 17 Optical path — view from above the instrument.

Table 5 Accumulated depositions after 72 h with sample at 80 °C.

$T_{collector}$		[μg cm^{-2}]	[%]	% of TML
80 K	TML[a]	288.421	0.04610	100.0
213 K	VCM[b]	2.128	0.00034	0.7
253 K	VCM	0.292	0.00005	0.1
293 K	VCM	0.008	<0.00001	0.0

[a]Total Mass Loss.

[b]Volatile Condensable Materials.

The EIS instrument was thoroughly tested. This was done first at component level and then using a full Mechanical Thermal Model (MTM) of the instrument. The MTM served to verify that the design met (a) the main mechanical requirements of stiffness and strength, (b) the main thermal requirements of thermal balance and stability and (c) stringent cleanliness requirements during manufacture, assembly, test and ability to survive limited periods of exposure to the environment.

The MTM structure was flight-like. The flight electronic and optical subsystems were represented by heaters and dummy masses. To verify the contamination control procedures, the MTM was treated exactly as the FM model for every step of manufacture, assembly and testing. Cleanliness was monitored with QCM sensors and witness mirrors which formed an integral part of the instrument.

The MTM was vibration tested at the UK Aldermaston facility since the mass of the vibration adaptor with the instrument mounted on its semi-kinematic suspension exceeded 500 kg. The test was limited at a frequency of 200 Hz. The higher frequency range was tested separately in an acoustic test. Strength was verified with sine bursts (5 cycles) at 12.5 g in the lateral and 19 g in the longitudinal directions. Half Sine Shock 16.7 $g_n$pk × 10 mS was performed in the longitudinal direction. All units mounted inside the structure were tested and qualified separately, based on the responses measured during the MTM testing. The first resonance measured was located at 59 Hz. This was only 1 Hz below the requirement and was therefore deemed acceptable.

At the end of the successful MTM test campaign, the cleanliness measurements showed that the rigorous cleanliness regime would result in an overall accumulated contamination for the flight instrument well below the required limits. Except during vacuum testing, the instrument was bagged and purged with dry nitrogen throughout the testing and integration phase. The bagging will be removed at the launch. However, purging with ultra clean nitrogen will continue when the spacecraft is mounted inside the fairing of the launch vehicle up to about two hours before the launch time.

5.2. Thermal Design

The Hinode spacecraft is in a 680 km Sun-synchronous polar orbit with the EIS instrument sun-pointed during normal operations. The instrument temperature requirements are summarized in Table 6. The temperature gradient in the entire base structure that forms the optical bench must be less than 10 °C when in operational mode. The spacecraft orbit will include short eclipses every 8 months, during which time the solar loading on the instrument will change and will thus affect the temperature gradients. In operational mode there is internal heating by the instrument units of about 14 W. This dissipation is almost equally spread between the MHC and the ROE units, but there is also a small dissipation of 0.02 W at the CCDs themselves.

A thermal design using Multi-Layer Insulation (MLI), heaters and radiators has been developed. This design and the related computer models have been validated with data from

Table 6 Summary of temperature requirements (°C).

Item	Survival		Operational	
	Lower	Upper	Lower	Upper
CCD	−100	60	−90	−40
Mirror	−10	40	−10	30
Grating	−10	40	10	30
Filter foil	−200	200	−55	150
MHC unit	−35	65	0	50
ROE unit	−45	65	10	40
Optical bench	−40	40	10	35
Other structure	−90	120	−80	90
HOP[a] actuators	−120	70	−60	70
Slit-slot mechanism	−35	40	10	30

[a]High output paraffin actuator.

thermal testing of the EIS. These models will be used to support EIS on-orbit activities. The instrument is thermally isolated from the spacecraft by low-conductance titanium mounts. Much of the instrument is insulated by MLI blankets having a black Kapton outer layer. The shroud and aperture of the instrument are left uncovered as is a 0.057 m^2 area of the instrument structure adjacent to the MHC unit, which was required to radiate excess heat dissipated by the electronics. Dedicated white-painted radiators are used for cooling the CCDs and the nearby ROE unit. The CCD radiator is connected to a particle shield, which is in turn attached to the CCDs via a strap made of stacked thin copper foils. Thus the particle shield remains colder than the CCDs, protecting them from contamination and radiated heat loads. The mass of the CCD cooling system was kept as high as practical to provide sufficient thermal inertia to minimize temperature variation around the orbit. The CCD radiator is 0.216 m^2 and is fitted to the outward-facing surface of the instrument by eight low-conductance A-frame legs made from Torlon. A shade is placed on the sunward side of the CCD radiator to prevent direct solar heating.

The instrument is fitted with both survival and operational heater circuits. The thermostatically controlled survival heaters are positioned to keep the mirror, grating, and CCDs within survival temperature limits when the instrument is non-operational. There are 12 operational heaters fitted to the optical bench which are used to maintain structure temperatures and gradients during operation. The maximum power budget for these operational heaters is 15 W. In addition there are decontamination or bake-out heaters near the CCDs and make-up heaters near the ROE and MHC units.

Two sets of temperature sensors are fitted to the instrument. The first set comprises 10 sensors and can be monitored by the spacecraft when the instrument is switched off. These show temperature status of critical items and provide the feedback mechanism for control of the survival heaters. The second set comprises about 30 sensors which are monitored by the instrument's MHC unit. A number of these are fitted to the optical bench to ensure a good knowledge of its temperature gradient.

Thermal design cases are derived by taking the extremes of the cold and hot parameters that the instrument may experience during the mission. The cold and hot thermal design cases for operational modes are summarized in Table 7. The hot case assumes the high solar loads experienced at winter solstice together with the degraded end-of-life (EOL) properties.

Table 8 presents a summary of the orbital temperature predictions for the operational cases. In the cold case, the optical bench falls below temperature requirements if heaters are

Table 7 Summary of cold and hot operational thermal analysis cases.

Description	Cold	Hot
Spacecraft interface temperature [°C]	−10	30
Solar flux [W m^{-2}]	1290	1421
Earth temperature [K]	248	260
Declination/deg	23.5	−23.5
Earth albedo	0.35	0.25
Beta angle[a]	56.8	71
Radiative properties[b]	BOL	EOL

[a]Angle between sun-vector and satellite orbit plane.

[b]BOL and EOL are beginning-of-life and end-of-life respectively.

Table 8 Temperature predictions for cold and hot operational cases.

Sub-system	Predictions [°C]	
	Cold	Hot
CCD	−58 to −55	−49 to −45
Mirror	19	18
Grating	15	15
Filter foil	6 to 124	134
MHC unit	18	21
ROE unit	29	30
Optical bench	15 to 22	15 to 22
HOP actuators	15 to 19	18 to 33
Slit-slot mechanism	15	16

Note: Range given if T varies by >2 °C around orbit or across an item.

not used. Therefore the operational heaters are required to warm the optical bench to ≈15 °C and to ensure that the gradient requirement is achieved. In the hot case, the optical bench is predicted to be at the lower end of the operational temperature range without heating. However, some heating is required to ensure that the gradient requirement is achieved. Optical bench heater dissipation is predicted to be ≈12 W in the cold case and ≈4 W in the hot case. Thus there is good margin with respect to the maximum allowable heater dissipation of 15 W.

6. Electronic Design

6.1. Mechanism and Heater Control

The EIS MHC unit consists of the Mechanism Driver Electronics (MDE) and the power subsystem. The Naval Research Laboratory produced the MDE and MSSL produced the MHC back plane, housing and power subsystem. The MHC system provides control of the grating focus mechanism, mirror coarse and fine motion mechanisms, shutter mechanism, slit/slot mechanism, twelve EIS operational heaters, and the two High Output Paraffin (HOP) actuators, each with redundant heater circuits, for opening the Clamshell doors. In addition, the MHC electronics drives two calibration LEDs, two Quartz Crystal Monitors (QCM) for contamination measurement, structure thermistors, an Entran vacuum gauge to check Clamshell pressure, Clamshell door encoders, and other housekeeping sensors within the instrument. The MHC is housed in a single aluminum alloy enclosure (Figure 18).

Figure 18 The MHC electronics box is housed in a single enclosure. Boards mounted in the box include the Digital Board (top row of connectors), Analog Board (second row), Auxiliary Board (third row) and the Power Converter Board (bottom connector).

The MDE includes the digital Printed Circuit Board (PCB), the analog PCB and the auxiliary PCB. A block diagram of the MDE is shown in Figure 19.

The digital PCB provides the interface to the ICU via a full duplex, 9600 byte/s, asynchronous RS-422 serial data interface. The control logic is driven by an 8085 radiation hardened microprocessor which also provides the serial input/output functions. The MHC software resides in a 32 k × 8 bit PROM which operates from MHC software uploaded from the ICU to a 64 k × 8 bit RAM device, switchable under software control. The digital PCB provides stepper motor logic for the grating focus mechanism, mirror coarse motion mechanism, and the slit/slot mechanism. It also provides the control logic for the shutter brushless DC motor. Stepper motor voltages are switched and passed to the grating, mirror, and the slit/slot mechanisms.

The analog PCB provides the analog to digital conversion functions, the mirror fine motion control, coarse mirror and slit/slot resolver to digital conversion, voltage and current monitoring, the Entran vacuum gauge operation and structure temperature monitoring. The mirror fine motion control is handled through a PZT drive circuit and a closed-loop strain gauge feedback loop.

The auxiliary PCB provides the operational heater and HOP control, feedback from the optical encoders on the inner and outer clamshell doors, a constant current source for the two calibration LEDs, and switched power to the QCMs and QCM heaters.

The MHC power subsystem provides appropriate electronics, motor, heater and PZT voltages to the MDE. The MHC power interface consists of three +28 V supplies: an electronic supply which provides MHC internal power and shutter power via the MHC power converter, a heater supply which powers structure heaters directly, and a motor supply which powers stepper motors and paraffin actuators. The MHC internal power is generated by two DC/DC converters. Two converters are used to decouple any noise generated on the digital
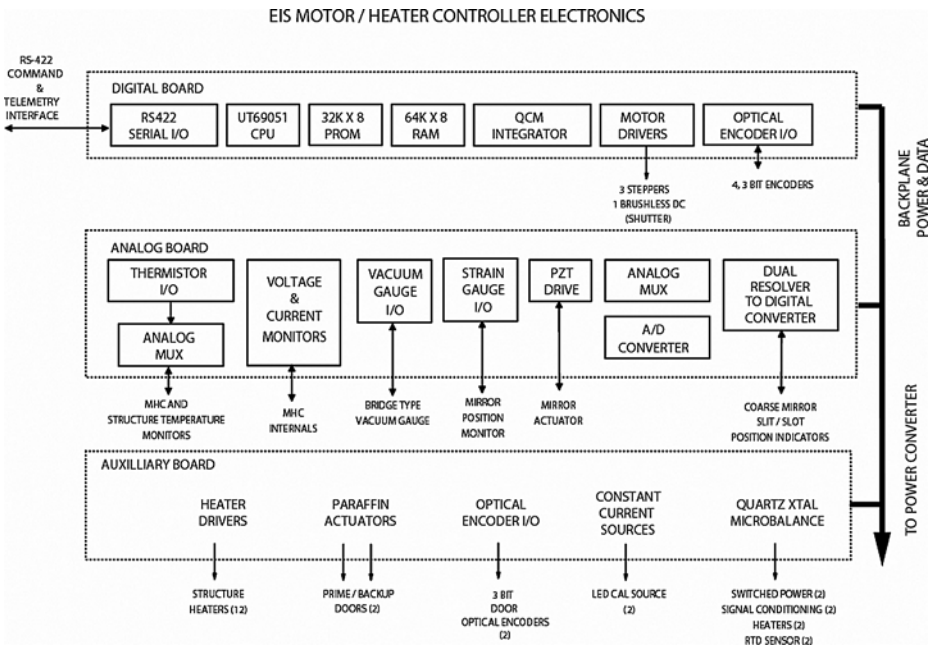
Figure 19 Simplified block diagram of the Mechanism Driver.

and mechanism supplies from the low noise analog supplies, thus enhancing the performance of the analog circuits.

The MHC responds to any of the 35 pre-defined commands issued from the ICU via the RS-422 data link. There are two types of response from the MHC to a command: (a) commands that require a data response (memory dump, housekeeping, *etc.*) will be acknowledged by the return of data if successful, or a Not Acknowledged (NAK) signal in case of failure; (b) commands not requiring a return of data will be recognized by a brief Acknowledged (ACK) signal on successful command completion or a NAK signal for command failure. The MHC does not initiate any data transfer. Commands are not queued by the MHC and a command received while a prior command is pending will generate an error (NAK). The only commands that will be executed while another command is being processed are the ABORT, RESET, and SAFE commands. There are 125 parameters associated with the MHC (heater duty cycles, auto safe parameters, mirror and slit/slot resolver values, *etc.*). Embedded in the flight software is a set of default values assigned to each of these 125 parameters. Using the PARAMETER_SET command, each of the parameters can be changed in-orbit to values within a pre-determined range.

The MHC has three operating modes: Safe, Idle, or Command Active. Following power-up, the MHC is put in the Safe operating mode. In this mode, use of the shutter, coarse mirror, grating, and slit-slot mechanisms are prohibited and any command that attempts to drive these mechanisms will be rejected, *i.e.*, a NAK response will result. All other commands will be accepted and processed normally. The Safe operating mode can also be entered either by command or autonomously. Either a SAFE command or a RESET command will cause the MHC to enter the Safe operating mode. To enter the Idle operating mode, the MOTOR_ENABLE command is issued by the ICU. The Idle operating mode is the MHC state from which all commands are accepted. The Command Active operating mode is en-

tered following the receipt of a valid command from either the Safe or Idle modes. When the MHC is in the Command Active mode, only the ABORT, RESET, or SAFE commands are accepted, all others are rejected. The MHC will transition from the Command Active mode to the Idle or Safe mode following completion of the current command.

The MHC supports two memory modes; Programmable Read Only Memory (PROM) mode and Random Access Memory (RAM) mode. In PROM mode, the baseline code residing in a PROM is executed. In RAM mode, the program currently loaded in a RAM is executed. The baseline code is copied from PROM to RAM at power-up. On power-up, the default is PROM mode. Switching between modes is accomplished via the MEMORY_MODE command and always results in a return to the SAFE operating mode. Updated MHC operating code can be uplinked from the ICU to the MHC RAM using the MEMORY_UPLOAD command.

6.2. On-Board Data Processing Unit

The ICU is an on-board processor that controls the entire EIS instrument. Located in the spacecraft bus section, it also handles interfacing between the EIS spectrometer and the spacecraft. Figure 20 gives an overview of the ICU electronics. The circuitry is located on five printed circuit boards: spacecraft interface and processor board, camera and mechanism controller board, analog monitor board, power supply unit and a backplane. The spacecraft interface and processor board is based around a TEMIC 21020 Digital Signal Processor (DSP) running at a clock speed of 20 MHz. There are two FPGAs, a Static RAM (SRAM; 1 Mb) and a boot PROM of 8 kb to support the DSP. One FPGA decodes the address space for the memory and I/O. It also implements the Watch Dog and Spacecraft timer functions and a "boot-strap" code power-up function. The second FPGA deals with the spacecraft digital interfaces.

The spacecraft interface is based on three links, command and housekeeping or status, both 62.5 kbps and science mission data transfer at 2 Mbps. Each of the interfaces incorporates First In First Out (FIFO) buffers. The camera and mechanism controller board contains onboard application code storage in 1 Mb of Electrically Eraseable PROM (EEPROM) which can hold two versions of the code, CCD image buffers in 4 Mb of SRAM for the raw science data and two further FPGAs. One FPGA handles the 32 Mbps high speed link between the ROE and the ICU while the second controls the RS422 9.6 kbps interfaces between the ICU and the ROE and MHC. The analog monitor contains the primary power interface and current limiter for the instrument. It is responsible for temperature, current and voltage monitoring, primary and secondary line switching and heater switching. FET switches are used to switch primary power to the MHC, bake-out and substitution heaters and secondary unregulated power to the ROE. An FPGA is used for control of the monitoring function and bus interface along with an ADC, analog multiplexers and operational amplifiers. Secondary power line conditioning is provided by the power supply unit board. There are regulated power lines for the ICU and unregulated ones for the ROE. The backplane provides the interface connections between the above boards.

Buffer logic on the daughter boards for the backplane is included in the FPGAs but is not shown in the diagram. The bootstrap code in PROM is written in assembly language and supports the loading and dumping of the operational code from either bank of the EEPROM or spacecraft to RAM, as commanded. In order to facilitate the software development the operational code is designed to be modular. This code is written in C operating under the
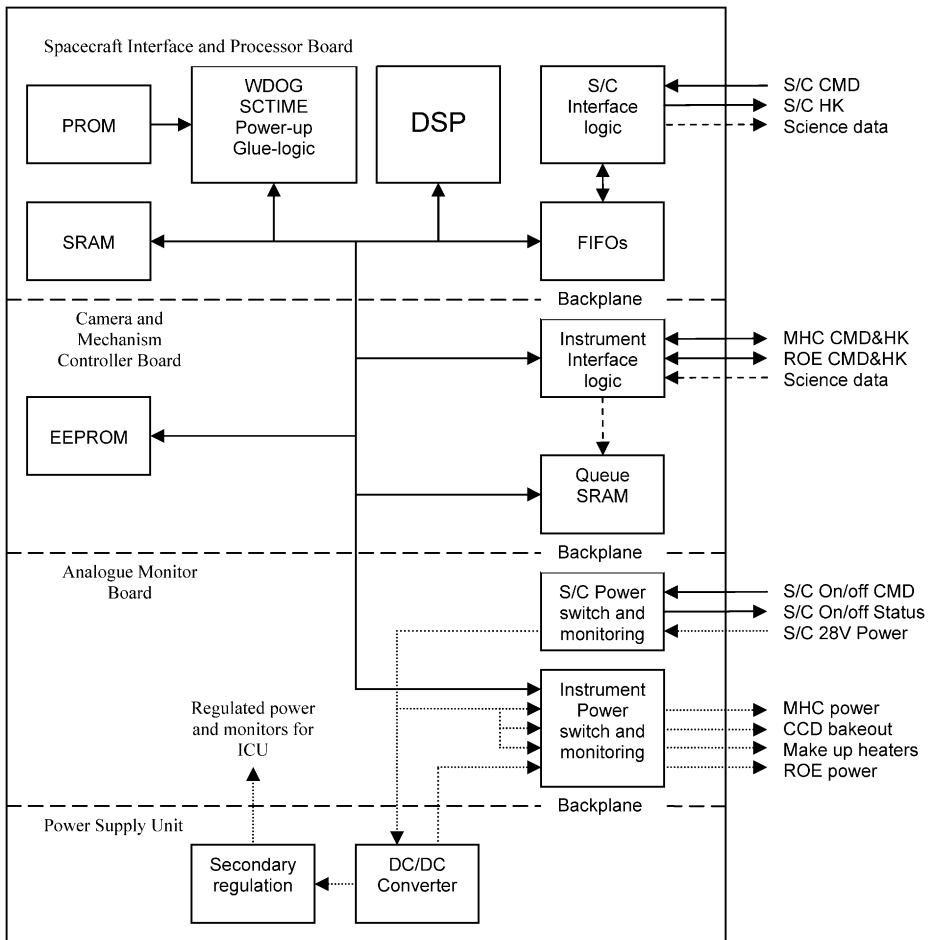
Figure 20 Block diagram for the EIS Instrument Control Unit.

Virtuoso real-time operating system (Wind River Inc.). This is necessary to support the spacecraft and instrument requirements for task scheduling and inter-task communication.

An overview of the EIS software modes is given in Figure 21. Boot mode is used to load, dump and run the main application programme. The boot code also supports housekeeping requests. Standby mode is the first mode entered after invoking the application code. In this mode only the ICU and "make up" heaters in the ROE and MHC are powered. In manual mode the ROE and MHC are powered and the instrument can be fully configured ready for science operations. Science sequences are loaded into memory from the ground and the next sequence to be run is selected. In auto mode, sequences are run together to form a complete science observation or study. When a study is complete, the instrument can be commanded back to manual mode and the first sequence of the next study selected.

Bake-out mode is used to decontaminate the CCDs. A closed loop heater controller warms the CCDs in a controlled fashion to the bake-out temperature where the selected value is held. Likewise the CCDs are allowed to cool at a controlled rate after the bake-out is complete. From any of the above application code modes, emergency mode can be en-
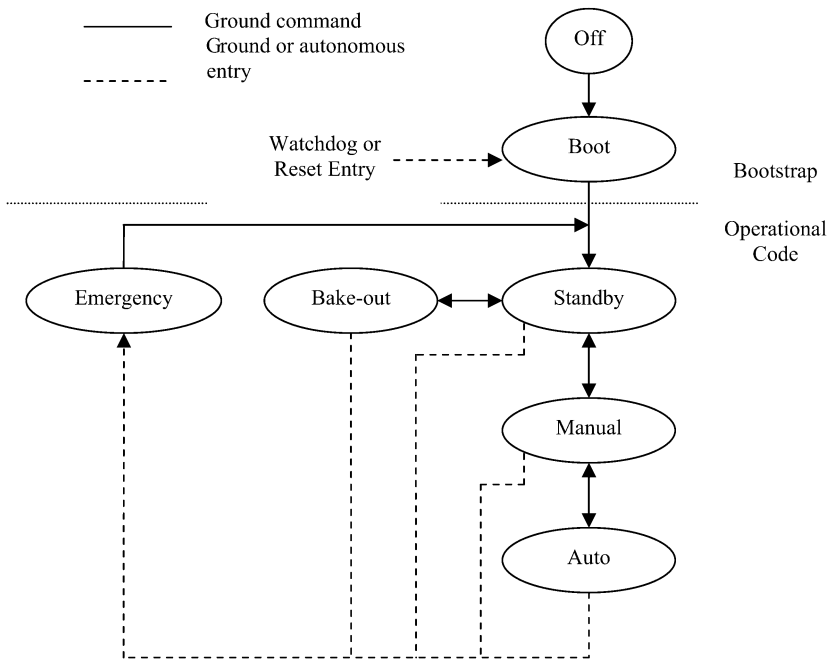
Figure 21 Diagram showing the operation of the EIS on-board software.

tered either by command or by the instrument health monitor software module. The health monitor checks for two consecutive values of a parameter exceeding a defined limit. Parameter limits are loaded from the ground, except for default values for the maximum CCD temperatures. The parameters checked are currents, voltages and temperatures. Emergency mode can also be entered if communication with the MDP or MHC is lost for any reason.

7. Instrument Calibration and Performance

The laboratory calibration of EIS follows the successful example of CDS (Lang *et al.*, 2000). The instrument was calibrated just prior to final hardware delivery. The EIS entrance aperture was illuminated with EUV radiation and a series of calibration images obtained. The calibration comprised an end-to-end test of the entire EIS instrument.

Two EUV light sources were used. One was a Penning discharge lamp (Finley *et al.*, 1979, Berkeley Photonics Inc.) which, at the focus of a custom-built collimator illuminated fully the EIS aperture. This laboratory light source was used to focus the spectrometer and to obtain the wavelength calibration. The other source was a secondary radiometric standard (Hollandt *et al.*, 2002), a hollow-cathode lamp combined with a collimating telescope, previously calibrated against the electron storage ring BESSY I as a primary standard of calculable synchrotron radiation (Ulm and Wende, 1997). This source beam was 5 mm in diameter and did not fill the EIS aperture. The instrument aperture response was computed by obtaining successive exposures over the aperture. The overall effective area of the EIS instrument was a weighted average of the efficiency. The laboratory calibration of EIS is described in detail elsewhere (Lang *et al.*, 2006) so only a brief account is given here. The calculated instrument response to three typical solar coronal spectra is also presented.

7.1. Wavelength Calibration

The instrument was fully assembled at the Rutherford Appleton Laboratory in the UK and aligned in its flight configuration. Tests with the Penning EUV discharge lamp were performed with the instrument in a high vacuum facility. A 150 mm diameter multilayer coated spherical mirror was used to collimate the radiation from the Penning lamp and fill the EIS telescope aperture to permit optimal focusing. The lamp was operated with He or Ne gas and Mg electrodes. Representative spectra recorded with a 10 μm slit are shown in Figure 22 for the long wavelength band using neon. Figure 23 shows representative spectra from the short wavelength band from ionized magnesium and neon. Figure 24 shows a He II 256 Å line profile with a Gaussian fit also indicated for both linear and log scales. The FWHM He line width is 0.056 Å or 2.5 pixels for a measured spectrometer resolving power of $\lambda/\Delta\lambda = 4570$ at this wavelength. Many of the spectral lines observed are found in the NIST database (2005) and in Kelly's compilation (Kelly, 1987), but a number of new lines of Ne II, III, and IV were identified in the course of this work (Kramida *et al.*, 2006; A.E. Kramida, 2006, private communication; C.M. Brown, 2006, private communication), a tribute to the high resolution and sensitivity of EIS. One minute (long wavelength band) and 5 minute (short wavelength band) exposures were recorded using the 1 arc sec slit.

Spectral images were formed in the upper half of each CCD, just above the midline. For these images 50 rows were averaged to produce a spectral intensity curve. These intensity

Figure 22 Neon and Magnesium long λ Penning discharge spectrum recorded with the EIS spectrometer.
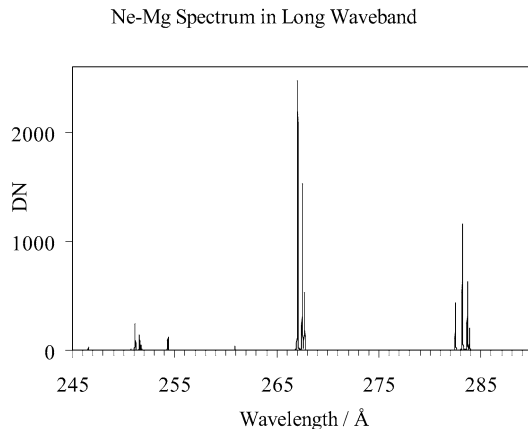

Figure 23 Representative short λ Ne-Mg spectra recorded with the EIS spectrometer.
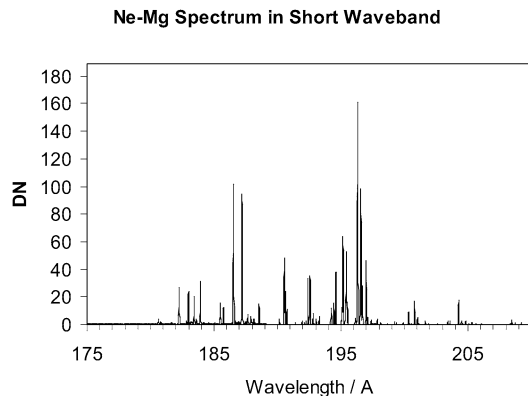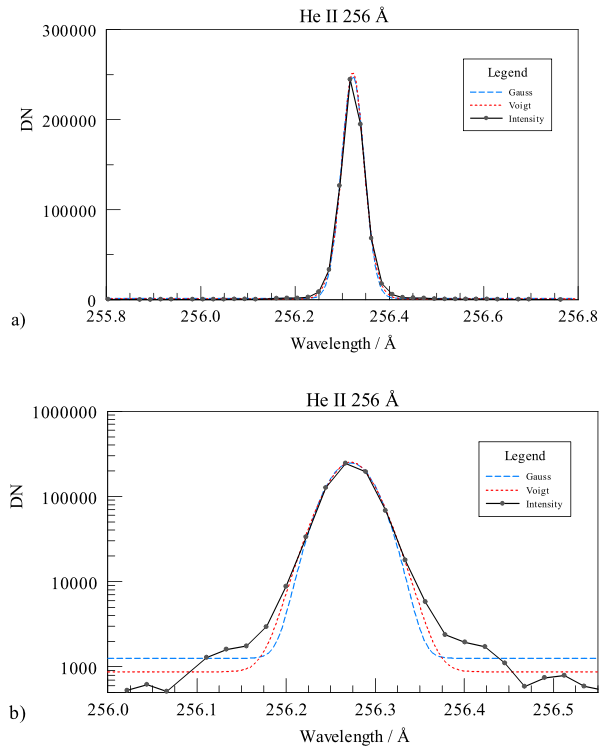
Figure 24 Profile of the He II 256.32 Å spectral line from a Penning discharge lamp, as recorded by EIS on (a) linear and (b) semi-log scales. Also shown are fitted Gaussian (blue) and Voigt (red) line profiles. The fitted FWHM for the Gaussian profile is 0.056 Å.

curves were measured using the Gfit program (Engström, 1998) to fit Gaussian shapes to the line profiles. Line positions were determined to ≈0.1 column accuracy for good lines, and the FWHM of unblended lines was typically 2.5 pixels. The area under the Gaussian curve was also computed by the program.

This list of measured lines was then compared with a list of standard lines and fitted with the lowest order polynomial practical. In general, no improvement in fit was found for orders higher than second. The dispersion function for the long wavelength band results from a second order polynomial fit to the data from 32 standard lines and is given by

$$\lambda(p) = \lambda_0 + Ap + Bp^2 \tag{1}$$

where p is the pixel (or column) number and λ_0, A, and B are the polynomial coefficients. Here, $\lambda_0 = 199.9389$ Å, with $A = 0.022332$ and $B = -1.329 \times 10^{-8}$ while the standard deviation was 0.00415 Å. λ_0 can be interpreted as the wavelength of the edge of column 0 for each detector. A is the linear term in Å/pixel. Figure 25 shows a plot of the reference wavelength minus the fitted wavelength for this detector. Likewise, for the short wavelength band using the format of Equation (1), the polynomial coefficients are: $\lambda_0 = 166.131$ Å, $A = 0.022317$ and $B = -1.268 \times 10^{-8}$. The standard deviation of the fit was 0.00386 Å. Figure 26 shows a plot of the deviations of the fitted wavelengths from the standard wavelengths of 65 lines.

Figure 25 Wavelength
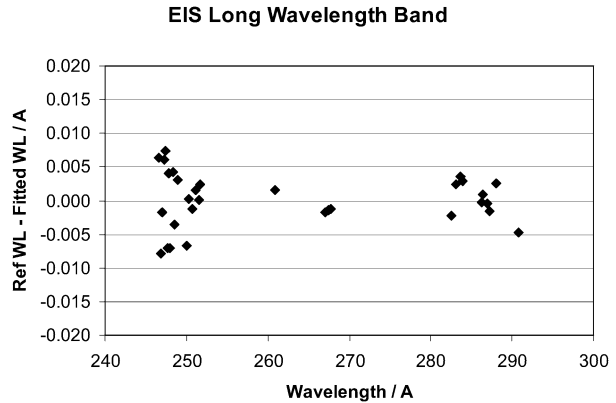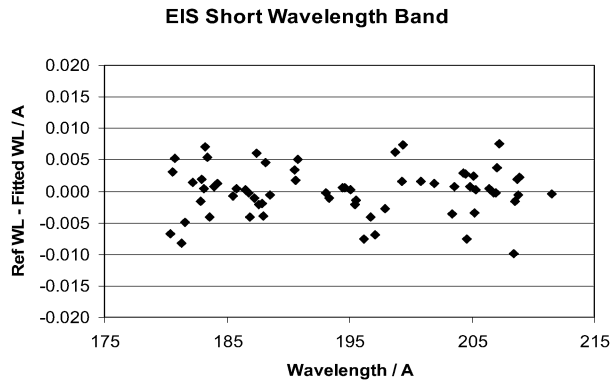deviations for standard lines; EIS
long wave band.

EIS Long Wavelength Band

Figure 26 Wavelength
deviations for standard lines; EIS
short wave band.

EIS Short Wavelength Band

7.2. Effective Aperture Determination

The geometric aperture of the mirror and grating combination may be calculated from accurate mechanical drawings. In addition, allowance must be made for the obstructions associated with the entrance filter structure and filter support frame. The vignetting of the long wavelength (LW) CCD by the slit/shutter housing must also be calculated. This housing causes wavelength dependent vignetting of the radiation from grating to the detector for wavelengths greater than 272 Å and was measured during the radiometric calibration. The housing also vignettes the beam incident on the grating for some mirror positions. The mirror aperture is shown as a function of coarse mirror position in Figure 27. Details are given by Lang *et al.* (2006).

For measurements in the vacuum chamber, the calibrated high current hollow cathode lamp (Danzmann *et al.*, 1988) emits unpolarized line radiation from the carrier gas (Ne or He) and from sputtered cathode material (99.5% Al). The lamp illuminated a pinhole at the focus of a Wolter type II telescope while a 5 mm aperture stop placed just after the telescope mirror defined the collimated output beam. This telescope polarizes the output beam. The output of the source is the measured sum of the different polarization outputs (Hollandt *et al.*, 2002; Hollandt, 1994). However, it is known that polarization effects are not appreciable at normal incidence, *e.g.*, Samson (1967), and as EIS is a normal incidence instrument, polarization effects can be ignored. The aperture was scanned from one edge of

Figure 27 Mirror aperture as a function of coarse mirror position. The small fall-off in area for the LW aperture from 6 mm to 10 mm results from vignetting by the slit/shutter housing.
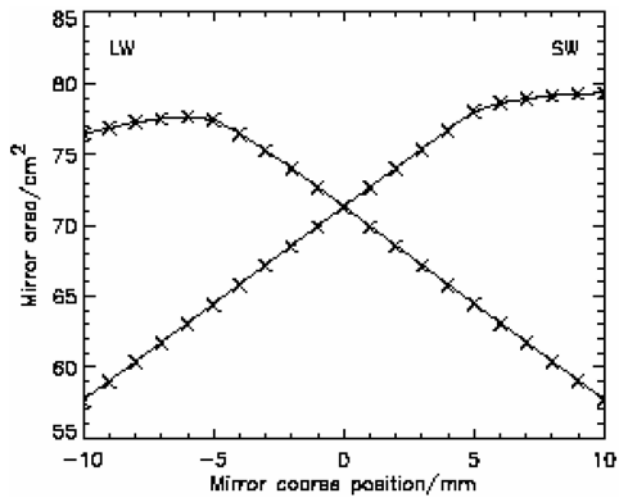

Table 9 Source calibration line list.

Wavelength [Å]	Spectrum	Photon flux [photons s^{-1}]	Last calibration uncertainty (1σ)	Aging uncertainty (1σ)
204.3 – 208.9	Ne III	3.43×10^5	8%	10%
251.1 – 251.7	Ne III	4.39×10^5	"	"
256.3	He II	8.53×10^6	"	"
276.1 – 267.7	Ne III	1.01×10^6	"	"
282.5 – 283.9	Ne III	2.61×10^6	"	"

the mirror to the other by moving EIS horizontally in 10 mm steps on its translation table between exposures.

After each horizontal scan, the calibrated source was moved up or down nominally by 10 mm and the horizontal scan repeated to map the whole aperture. With helium as the hollow cathode base gas, only the He II 256.3 Å line could be used to illuminate the long wavelength part of the aperture. With neon as the base gas, numerous lines were observed in both the EIS bands and the scan was over the full aperture. The radiometrically calibrated ranges together with the output fluxes and uncertainties are given in Table 9.

Prior to final instrument assembly, mirror and grating reflectivities and entrance and slit filter transmissions were measured at the Brookhaven Synchrotron Light Source (Seely *et al.*, 2004). Measurements for these subsystems are shown in Figures 28 and 29 along with previously estimated values. The flight grating groove depth, the most demanding of the grating specifications to achieve, has a measured value of 67 Å compared with the specified value of 60 ± 4 Å. This small added depth moves the peak groove efficiency to longer wavelength by $\approx$20 Å and slightly affects the resulting response curves. Another factor in the comparison is that a fixed groove efficiency of 35% was used whereas the efficiencies estimated using the achieved groove depth vary between 30% and 40% with wavelength for the short wavelength band.

The measured and estimated transmission of the slit filter, including its supporting mesh, is plotted as a function of wavelength in Figure 29. The previously estimated filter transmis-

Figure 28 Measured and
predicted values for the product
of flight mirror and grating
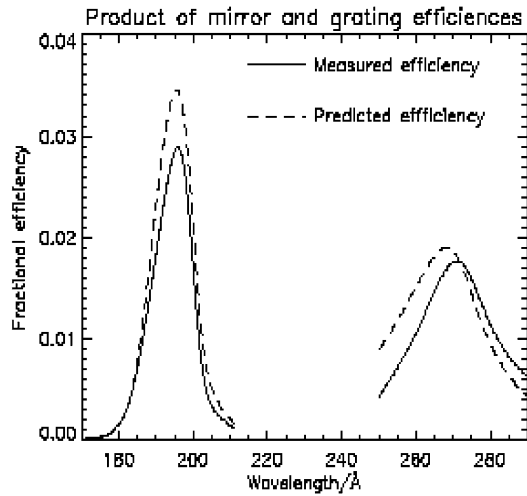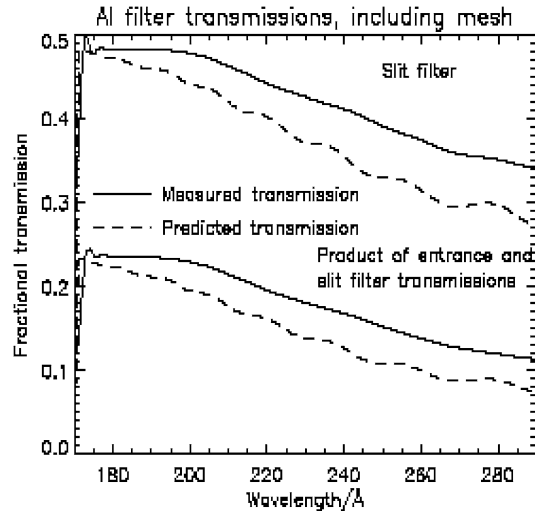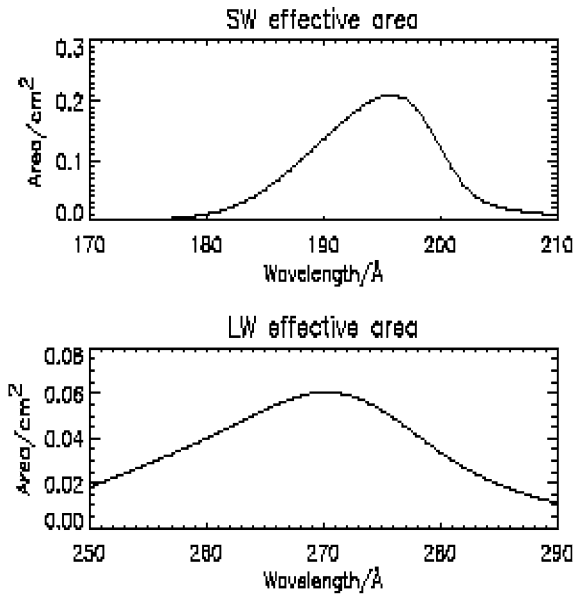reflection efficiencies.

Figure 29 Measured and
predicted values for the slit filter
transmission and for the product
of entrance and slit filter
transmissions.

sion was based on a thickness of 1500 Å aluminum with a 75 Å Al_2O_3 layer on each side. The measured filter transmission is best fitted by 1500 Å aluminum with 80 Å Al_2O_3 layers on each side. However, more recently available values of Al and Al_2O_3 optical constants were used for fitting the measured transmissions. The products of the transmissions for entrance and slit filters are also shown in Figure 29. The entrance filter was not included in the end-to-end calibration measurement of the instrument but was fitted to the EIS instrument shortly before the launch of Hinode.

The detector quantum efficiency (QE) used in the original instrument sensitivity estimate presented by Lang, Kent, and Seely (2002) was 0.8 based on measurements on CCDs with "UV enhanced" backside treatments by the CCD manufacturer (Stern *et al.*, 2004). However, the CCDs chosen for EIS did not have the enhanced treatment and are expected to have a 25 to 40% lower QE. The QE values of two engineering quality CCDs of the EIS type were measured using synchrotron radiation and the same apparatus as used to mea-

Figure 30 The SW and LW effective areas based on measurements of the efficiencies of the individual optical elements (filters, mirror, grating, CCDs) of EIS. Vignetting in the LW band by the slit and shutter housing is also included.

sure the flight mirror and grating reflectivities. For the short-wavelength band the measured efficiencies averaged 48% and 40% and for the long-wavelength band were 42% and 35% respectively. These CCDs were from the same batch but a different wafer from those chosen for flight. Noting the variation in the measured results, it was decided to use the average of the measurements for the EIS calibration model. The CCD quantum efficiencies adopted were $44 \pm 4\%$ for the short wavelength band and $40 \pm 4\%$, $39 \pm 4\%$ and $37 \pm 4\%$ at the longer wavelengths of 250 Å, 270 Å, and 290 Å, respectively. These efficiencies can be combined to give the predicted effective areas for the two EIS wavelength bands, as shown in Figure 30.

In applying the laboratory calibration to solar observations, the change of illumination from a small source filling a small part of the aperture to full solar illumination must be allowed for as well as the effect of making a coarse movement of the mirror. The conversion from data numbers/sec to radiance (I_λ) can be made using Equation (2)

$$I_\lambda = (D_\mathrm{L}/D_\mathrm{p})(1/A)(1/A_\mathrm{s})\big((180.0 \times 60.0^2)/\pi\big)^2 \text{ photons cm}^{-2}\,\text{s}^{-1}\,\text{sr}^{-1} \qquad (2)$$

where A is the aperture area in cm^2 and A_s is the area of the spectrometer slit or slot illuminated by the source in arc sec^2. D_L is the digital signal in a spectrum line measured in data numbers at the output of the camera ADC. To relate the data numbers to the number of detected photons, the number of electrons was calculated using the electron-hole pair creation energy of silicon ((3.66 ± 0.03) eV at room temperature (Scholze *et al.*, 2000) corresponding to (3.68 ± 0.04) eV at 215 K (Canali *et al.*, 1972; Sze, 1981), the operating temperature of the CCDs) and the incident photon energy and then converted to data numbers using the gain of the camera (6.60 ± 0.03 electrons per data number).

The factor D_p, the responsivity measured during the end-to-end calibration of EIS, is obtained by dividing the measured data number values corresponding to the calibration wavelength ranges by the appropriate calibrated source output as given in Table 9. Predicted

responsivities are derived from the effective areas based on the measurements for the individual elements as shown in Figure 30. As the predicted responsivity is based on flight unit results apart from the CCDs where engineering model devices were used for the Brookhaven SLS measurements, the final responsivity for EIS must reconcile the end-to-end with the predicted measurements. The quantities involved for the standard source wavelength intervals are given in Table 10.

The normalizing factor (Norm = 1.60) was chosen to obtain agreement between the measured and predicted responsivity values for $\lambda = 267.25$ Å. The adopted long-wavelength band responsivity is the laboratory result with the normalized predicted responsivity scaled to give the measured responsivity at 251.3 Å and 283.4 Å. For the long-wavelength band, Figure 31 shows the responsivities as measured using the calibrated source (crosses with error bars), the predicted responsivity (dash-dot line), the normalized responsivity (predicted responsivity times 1.60; dotted line) and the adopted laboratory responsivity (solid line). The uncertainty in the laboratory responsivity is taken as the sum of the average uncertainty of the measured responsivities (15.6%) and the uncertainty of the predicted responsivity (13.3%), namely 20.6%, as indicated by the dashed lines in Figure 31.

For the short-wavelength band (see Table 10), the normalized predicted sensitivity is lower than the measured responsivity. The laboratory responsivity is taken as the measured result, extended to other wavelengths by matching the normalized predicted data to the mea-

Table 10 Line data numbers, responsivities and comparison with predicted values.

Band	λ [Å]	Data numbers [DN sec^{-1}]	Responsivity [DN/photon]		Meas./ pred.	Meas./ norm.
			Measured	Predicted		
LW	251.3	$8.54 \pm 1.00 \times 10^2$	$1.95 \pm 0.34 \times 10^{-3}$	$1.47 \pm 0.20 \times 10^{-3}$	1.32	0.83
LW	256.3	$2.77 \pm 0.28 \times 10^4$	$3.25 \pm 0.53 \times 10^{-3}$	$2.24 \pm 0.30 \times 10^{-3}$	1.45	0.91
LW	267.25	$6.70 \pm 0.50 \times 10^3$	$6.63 \pm 0.98 \times 10^{-3}$	$4.15 \pm 0.55 \times 10^{-3}$	1.60	1.00
LW	283.4	$8.30 \pm 0.51 \times 10^3$	$3.18 \pm 0.45 \times 10^{-3}$	$1.66 \pm 0.22 \times 10^{-3}$	1.92	1.20
SW	205.9	$8.95 \pm 0.80 \times 10^2$	$2.61 \pm 0.41 \times 10^{-3}$	$1.31 \pm 0.18 \times 10^{-3}$	1.98	1.24

Figure 31 The measured long wavelength band responsivity compared with predicted values. The points and curves are as described in the text.
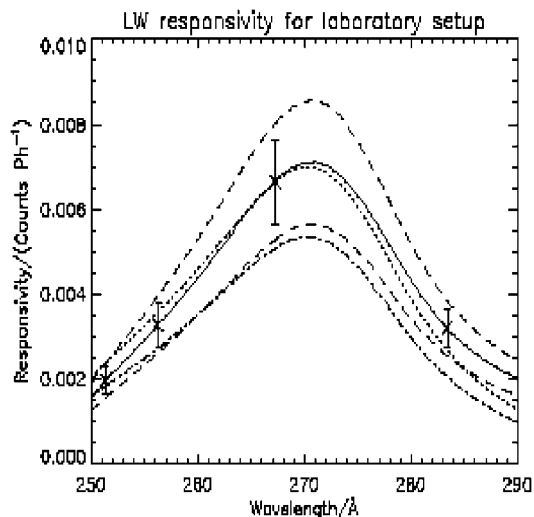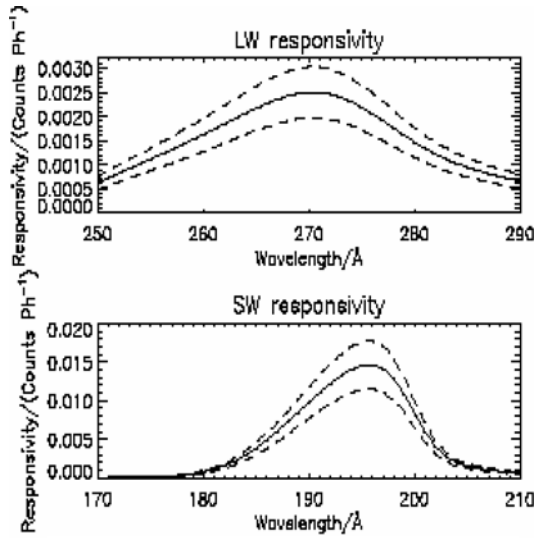
Figure 32 The long and short wavelength responsivities, D_p, as deduced from the calibration measurements. Dashed lines indicate the range of uncertainty.

sured result. Again the uncertainty in the result is taken as the sum of the uncertainties in the measured and predicted responsivities, namely 20.5%. Final measured responsivities are plotted against wavelength in Figure 32 for both the EIS bands and include the front filter transmission which has uncertainty 5%. If the normalizing factor of 1.6 at 267 Å (see Table 10) were ascribed entirely to CCD quantum efficiency, the figure of 39% measured in the Brookhaven CCD sub-system test should be increased to 59%. This is very similar to the QE value of 60% that was measured for the XRT CCDs at this wavelength (Hara, 2003; Sakao *et al.*, 2004). The XRT CCDs have an identical specification to the EIS flight devices.

When additional uncertainties of 2%, 4%, and 4% are added to allow for the uncertainties in the slit area, the mirror area, and for variations due to the spread of measurements of the QE of the engineering model CCDs, respectively, the overall relative standard uncertainty in the absolute responsivity calibration is 22%.

7.3. Instrument Performance

For an ideal optical system with no losses, the number of photons of wavelength λ entering the slit per second in a height interval corresponding to one pixel in the spatial dimension on each CCD, $N_{\text{slit}}(\lambda)$ is given by

$$N_{\text{slit}}(\lambda) = \phi_\lambda A \left(a/f^2 \right) \tag{3}$$

where ϕ (photons cm^{-2} s^{-1} sr^{-1}) is the intensity of the solar radiation, A (cm^2) is the mirror area, a (cm^2) is the area of the slit corresponding to one spatial CCD pixel in height times the width of slit, and f is the focal length of the mirror. These photons are then imaged onto the CCD in a manner determined by the magnification in the spectrometer section of the instrument. Thus, the number of photons per second registered on a pixel of each CCD is given by

$$N_\lambda = \phi_\lambda A \left(a/f^2 \right) (1/n_{\text{pix}}) \tag{4}$$

where the division by n_{pix} provides the desired solid angle per detector pixel. The design goal was to have the narrow slit match the pixel size. However, the actual slit widths result

Table 11 Quiet sun count rates (s^{-1} pixel^{-1}).

Ion	λ [Å]	Log T [K]	Incident	Detected	DN
Short wavelength					
Fe X	184.54	6.00	13.09	0.86	2.28
Fe VIII	185.21	5.60	8.87	0.69	1.84
Fe XII	186.88	6.10	13.97	1.60	4.21
Fe XI	188.23	6.10	17.87	2.65	6.91
Fe XII	193.52	6.10	29.06	8.13	20.60
Fe XII	195.12	6.10	48.15	14.58	36.63
Fe XIII	196.54	6.20	6.44	1.95	4.85
Fe XII	196.65	6.10	6.43	1.93	4.82
Fe XIII	202.04	6.20	18.02	1.49	3.60
Long wavelength					
He II[a]	256.32	4.90	18.50	1.04	1.98
Si X	258.37	6.10	13.54	0.88	1.66
Fe XIV	264.79	6.30	17.41	1.65	3.05
Si VII	275.35	5.80	9.35	0.89	1.59
Si VIII	277.06	5.90	8.36	0.71	1.25
Fe XV	284.16	6.30	68.25	2.77	4.78

[a]Intensity is a factor two higher than the CHIANTI value; see text.

in a need for small corrections. For the narrow slit (nominally 1 arc sec wide), the correction factor, n_{pix} is 1.067 and 1.087 for detectors A and B, respectively. The corresponding values for the 2 arc sec slit are 2.080 and 2.119. Note that the combination of factors results in the same solid angle per detector pixel, ω_d.

In practice, the actual number of registered photons will be reduced by additional factors due to the transmission of the two aluminum filters, the reflectivity of the mirror, the efficiency of the grating, and the quantum efficiency of the detectors (see Figure 1). Thus, the basic expression for the number of photons registered in each detector pixel per second is

$$N_\lambda = \phi_\lambda A \omega_d T_{ff}(\lambda) T_{spider} R_m(\lambda) E_g(\lambda) V_d(\lambda) T_{rf}(\lambda) E_{det}(\lambda) \tag{5}$$

where $T_{ff}(\lambda)$ and $T_{rf}(\lambda)$ are the transmissions of the aluminum front filter assembly and spectrometer entrance filter respectively; T_{spider} is the fractional area of the front filter assembly that is blocked by supporting structural members; $R_m(\lambda)$ is the reflectivity of the mirror coatings; $E_g(\lambda)$ is the grating efficiency which includes both the groove efficiency and the reflectivity of the multi-layer coatings, $V_d(\lambda)$ is a vignetting factor to account for the vignetting at the long-wavelength end of the long-wavelength detector and $E_{det}(\lambda)$ is the detector quantum efficiency.

The response of the EIS instrument to a range of solar conditions has been calculated using synthetic spectra from the CHIANTI data base (Version 4: Dere *et al.*, 1997; Young *et al.*, 2003). For line emission from an optically thin plasma, the intensity is

$$I_\lambda = \int G(T) \mathrm{DEM}(T) \, dT \text{ photons cm}^{-2} \text{ s}^{-1} \text{ sr}^{-1} \tag{6}$$

Table 12 Active region count rates (s^{-1} pixel^{-1}).

Ion	λ [Å]	Log T [K]	Incident	Detected	DN
Short wavelength					
Fe X	184.54	6.00	147.56	9.68	25.71
Fe XII	186.85	6.10	186.61	21.29	55.86
Fe XII	186.88	6.10	253.87	29.16	76.49
Fe XI	188.23	6.10	261.35	38.80	101.04
Fe XI	188.30	6.10	99.28	14.91	38.82
Fe XII	192.39	6.10	206.05	52.70	134.26
Fe XI	192.83	6.10	55.93	14.85	37.75
Fe XII	193.52	6.10	548.26	153.43	388.63
Ca XIV	193.87	6.50	24.62	7.05	17.82
Fe XII	195.12	6.10	907.96	274.93	690.66
Fe XII	195.13	6.10	89.64	27.15	68.20
Fe XIII	196.54	6.20	147.64	44.60	111.24
Fe XII	196.65	6.10	116.40	35.03	87.31
Fe XIII	197.43	6.20	48.21	13.82	34.30
Fe XIII	200.02	6.20	180.32	31.27	76.62
Fe XIII	201.13	6.20	203.14	24.05	58.60
Fe XIII	202.04	6.20	439.19	36.18	87.78
Fe XIII	203.83	6.20	749.17	32.72	78.68
Long wavelength					
He II[a]	256.32	4.90	58.38	3.26	6.24
S XIII	256.68	6.40	143.76	8.26	15.78
Fe XIV	257.39	6.30	158.04	9.56	18.20
Si X	258.37	6.10	249.17	16.11	30.56
Fe XVI	262.98	6.40	154.60	13.29	24.78
Fe XIV	264.79	6.30	543.86	51.43	95.20
Fe XIV	270.52	6.30	250.65	27.82	50.41
Fe XIV	274.20	6.30	396.32	40.28	72.01
Fe XV	284.16	6.30	3229.59	131.12	226.17

[a]Intensity is a factor two higher than the CHIANTI value; see text.

where $G(T)$ is the emissivity function but includes the temperature-independent parameters and DEM (T) is the differential emission measure function. Using CHIANTI V4 data and assuming a constant pressure of 10^{16} cm^{-3} K, $G(T)$ was calculated for all emission lines in the EIS wavelength bands. The $G(T)$ data and the CHIANTI DEM curves for quiet Sun, active region and flare cases were then used to compute spectra.

Using the synthetic spectra and the effective areas, we can calculate the number of photons registered in each detector pixel per second as

$$N_\lambda = I_\lambda A_{\text{eff}}(\lambda)\omega_d \tag{7}$$

where $A_{\text{eff}}(\lambda)$ is the effective area which includes all of the factors from Equation (5) except for ω_d which is the solid angle per pixel. Use of the appropriate values of D_p, then allows the

Table 13 Flare count rates (s^{-1} pixel^{-1}).

Ion	λ [Å]	Log T [K]	Incident	Detected	DN
Short wavelength					
Fe XXI	187.92	7.00	34298.14	4822.71	12579.11
Fe XI	188.23	6.10	9368.79	1391.00	3622.25
Fe XXIV	192.03	7.20	189315.64	46799.19	119458.12
Fe XII	192.39	6.10	7626.77	1950.48	4969.30
Ca XVII	192.82	6.70	219452.22	58220.96	148003.11
Fe XII	193.52	6.10	20345.04	5693.67	14421.38
Ca XIV	193.87	6.50	8714.48	2494.83	6307.85
Fe XII	195.12	6.10	33682.56	10198.99	25621.28
Fe XIII	196.54	6.20	6142.33	1855.63	4627.89
Fe XII	196.65	6.10	4241.22	1276.29	3181.27
Fe XIII	200.02	6.20	7737.11	1341.60	3287.67
Ca XV	200.97	6.60	14209.02	1783.61	4350.19
Fe XX	201.05	7.00	12026.51	1468.70	3580.81
Fe XIII	202.04	6.20	19404.28	1598.67	3878.44
Fe XIII	203.83	6.20	32127.88	1403.17	3374.33
Fe XVII	204.65	6.70	61496.85	2164.85	5185.02
Long wavelength					
Fe XVI	251.06	6.40	66188.77	2345.63	4579.51
Fe XXII	253.17	7.10	32180.93	1399.04	2708.70
Fe XVII	254.87	6.70	66730.63	3344.69	6432.54
Fe XXIV	255.11	7.20	101716.30	5198.91	9989.00
He II	256.32	4.90	108063.31	6049.24	11568.22
S XIII	256.68	6.40	52808.81	3035.89	5797.33
Fe XVI	262.98	6.40	116130.12	9985.35	18611.88
Fe XXIII	263.77	7.10	91040.15	8175.54	15192.91
Fe XIV	264.79	6.30	31941.00	3020.41	5591.22
Fe XVII	269.41	6.70	14806.13	1631.17	2967.73
Fe XIV	270.52	6.30	15148.67	1681.29	3046.37
Fe XXI	270.57	7.00	29343.42	3256.82	5900.15
Fe XIV	274.20	6.30	24752.87	2515.86	4497.33
Fe XV	284.16	6.30	507595.53	20607.53	35546.88

corresponding DN values to be estimated. Results for a selection of these lines are given in Tables 11 (quiet Sun), 12 (active region) and 13 (flares). For the flare line table, an extended version of the CHIANTI V4 differential emission measure was used. Earlier calculations used a version that cut off at log $T = 7.4$ K and thus did not account properly for Fe XXIV line fluxes. More complete tabulations are available on the MSSL EIS Website in the EIS planning guide at the URL given below.[1] At the EIS spectral resolution, the registered photons are actually spread out over three or more pixels. The complete tables include those

---

[1]http://www.mssl.ucl.ac.uk/www_solar/solarB/espg.html.

lines with detected photon numbers greater than 0.5 (quiet), 6.0 (active region) and 1000.0 (flare) photons. These tables allow estimates of the time needed to detect a given number of photons in a spectrum line. CHIANTI intensities have been calculated for optically thin emission lines. However, in a paper considering solar minimum EUV irradiance (Warren, 2005), it was noted based on Skylab observational values that when allowance is made for optical depth effects, the He II line intensities should be increased by a factor two over the CHIANTI values. This has been done for the entries in Tables 11 and 12.

8. Conclusions

The EIS is designed to study the high temperature plasma in the Sun's corona and upper transition region in the temperature range from below 1 MK to 20 MK and above. It has 2 arc sec spatial resolution and a plasma velocity measurement capability of better than ± 5 km s^{-1} for integration times of $10 - 100$ s for active region emission lines. Line profile studies will allow non-thermal effects or turbulent conditions in the plasma to be recognized. It will in addition measure plasma temperature and density and allow the construction of differential emission measure functions for the broad temperature range mentioned above. Measurements of element and ion abundances, particularly in outflowing plasma, will also be made. EIS achieves the above capabilities through the use of matched optimized multi-layer coatings on the primary mirror and on a focusing toroidal diffraction grating together with photon detection by back thinned and illuminated CCDs of high quantum efficiency in the 170 to 290 Å wavelength range. The ten times greater effective area than that of previous instruments in this spectral range, coupled with a higher data rate than was available from the SOHO spectrometers, will allow higher cadence studies of transient phenomena to be undertaken.

Together with XRT, EIS will benefit from the enormous capability of the SOT with its ability to measure photospheric velocity and vector magnetic fields at an angular resolution of ≈ 0.25 arc sec. Activity at the solar surface (photosphere) along with sub-surface activity in the convection zone, controls the upper atmosphere (transition region/corona) through the dynamic behavior of the photospheric plasma and the emergence of magnetic field from below the Sun's surface. Field lines project into the high atmosphere where they control the existence of the hot ($T > 1$ MK) coronal plasma and are responsible for the violent transient phenomena, *e.g.*, solar flares and CMEs, that have important effects on the near-Earth environment. The Hinode instruments are geared towards understanding the magnetic connection between the photosphere and underlying convection zone, and the corona, with particular reference to the phenomena of solar activity: structures, dynamics, plasma heating and transient events, to the evolution of the quiet sun network and intra-network regions and to the transfer of energy into the solar atmosphere. EIS in particular will focus on the dynamic and thermal response of the corona to the changing magnetic and velocity fields of the photospheric and sub-photospheric layers of the Sun.

The small fields of view of the SOT and EIS instruments will require careful joint observation planning that will be conducted on a monthly basis. Meetings will focus on (i) strategic planning for observations in the next three-month period and (ii) more detailed plans for the following month, subject to modification in response to developing solar conditions. Proposals for the use of EIS to make joint observations as part of the Hinode payload should be addressed to eis_obs@mssl.ucl.ac.uk.

The advanced features of the EIS instrument will enable it to play a highly significant part in the Hinode mission alongside the unique Solar Optical Telescope with its velocity

and magnetic field observing capability together with the full-Sun context view provided at high time cadence by the high resolution X-ray telescope.

References

Antiochos, S., DeVore, C.R., Klimchuk, J.: 1999, *Astrophys. J.* **510**, 485.

Beutler, H.G.: 1945, *J. Opt. Soc. Am.* **35**, 311.

Born, M., Wolf, E.: 1964, *Principles of Optics*, 2nd edn., MacMillan, New York, p. 469.

Canali, C., Martini, M., Ottavani, G., Alberigi Quaranta, A.: 1972, *IEEE Trans. Nucl. Sci. NS-19*.

Culhane, J.L., *et al.*: 1991, *Solar Phys.* **136**, 89.

Danzmann, K., Günther, M., Fischer, J., Kock, M., Kühne, M.: 1988, *Appl. Opt.* **27**, 4947.

Dere, K.P., Landi, E., Mason, H.E., Monsignori Fossi, B.C., Young, P.R.: 1997, *Astron. Astrophys. Suppl.* **125**, 149.

Engström, L.: 1998, GFit Version 10.0. *Lund Reports on Atomic Physics*, LRAP-232, LTH, Lund. http://kurslab-atom.fysik.lth.se/Lars/Gfit/html/index.html.

Finley, D.S., Bowyer, C.S., Paresce, F., Malina, R.F.: 1979, *Appl. Opt.* **18**, 649.

Haber, H.J.: 1950, *J. Opt. Soc. Am.* **40**, 153.

Hara, H.: 2003, *FM XRT-S Calibration*, National Astronomical Observatory of Japan.

Harra, L.K., Sterling, A.: 2003, *Astrophys. J.* **587**, 429.

Harra, L.K., Gallagher, P.T., Phillips, K.J.H.: 2000, *Astron. Astrophys.* **362**, 371.

Harra, L.K., Mandrini, C.H., Matthews, S.A.: 2004, *Solar Phys.* **223**, 57.

Harrison, R.A.: 1997, *Solar Phys.* **175**, 467.

Harrison, R.A., *et al.*: 1995, *Solar Phys.* **162**, 233.

Hollandt, J.: 1994, Strahlungsnormale für die solare Spektroradiometrie im Vakuum-UV, Ph.D. dissertation, Technischen Universität, Berlin.

Hollandt, J., Kühne, M., Huber, M.C.E., Wende, B.: 2002, In: Pauluhn, A., Huber, M.C.E., von Steiger, R. (eds.) *The Radiometric Calibration of SOHO, International Space Science Institute Report SR-002*, ESA, Nordwijk, p. 51.

Innes, D.E., Inhester, B., Axford, W.I., Willhelm, K.: 1997, *Nature* **386**, 811.

Kelly, R.L.: 1987, *J. Chem. Phys. Ref. Data* **16** (Suppl. No. 1).

Klimchuk, J.A.: 2006, *Solar Phys.* **234**, 41.

Korendyke, C.M., *et al.*: 2006, *Appl. Opt.* **45**, 8674.

Kowalski, M.P., *et al.*: 1999, *Appl. Opt.* **38**, 6487.

Kramida, A.E., Brown, C.M., Feldman, U., Reader, J.: 2006, *Phys. Scr.* **74**, 156.

Lang, J., Kent, B.J., Seely, J.F.: 2002, In: Pauluhn, A., Huber, M.C.E., von Steiger, R. (eds.) *The Radiometric Calibration of SOHO, International Space Science Institute Report SR-002*, ESA, Nordwijk, p. 337.

Lang, J., *et al.*: 2000, *J. Opt. A: Pure Appl. Opt.* **2**, 88.

Lang, J., *et al.*: 2006, *Appl. Opt.* **45**, 8689.

Madjarska, M.S., Doyle, J.G., van Driel-Gesztelyi, L.: 2004, *Astrophys. J.* **603**, L57.

Masuda, S., Kosugi, T., Hara, H., Tsuneta, S., Ogawara, Y.: 1994, *Nature* **371**, 495.

Nakariakov, V.M., Ofman, L.: 2001, *Astron. Astrophys.* **372**, L53.

NIST Atomic Spectral Data Base: 2005, http://physics.nist.gov/cgi-bin/asd.

Pevtsov, A.A.: 2000, *Astrophys. J.* **531**, 553.

Powell, F.: 1992, In: Bennett, H.E., Chase, L.L., Guenther, A.H., Newman, B., Soileau, M.J. (eds.) *Laser-Induced Damage in Optical Materials*, *Proc. SPIE* **1848**, 503.

Sakao, T., *et al.*: 2004, In: Mather, J.C. (ed.) *Optical, Infrared, and Millimeter Space Telescopes*, *Proc. SPIE* **5487**, 1189.

Samson, J.A.R.: 1967, *Vacuum Ultraviolet Spectroscopy Techniques*, Wiley, New York, p. 315.

Scholze, F., Henneken, H., Kuschnerus, P., Rabus, H., Richter, M., Ulm, G.: 2000, *Nucl. Instrum. Methods* **39**, 208.

Schumacher, R.J., Hunter, W.R.: 1977, *Appl. Opt.* **16**, 904.

Seely, J.F., Brown, C.M., Windt, D.L., Donguy, S., Kjonrattanawanich, B.: 2004, *Appl. Opt.* **43**, 1463.

Stern, R.A., *et al.*: 2004, In: Fineschi, S., Gummin, M.A. (eds.) *Telescopes and Instrumentation for Solar Astrophysics*, *Proc. SPIE* **5171**, 77.

Sze, S.M.: 1981, *Physics of Semiconductor Devices*, 2nd edn., Wiley, New York, p. 754.

Tsuneta, S.: 1995, *Publ. Astron. Soc. Japan* **47**, 691.

Tsuneta, S.: 1996, *Astrophys. J.* **456**, L63.

Ulm, G. Wende, B.: 1997, In: Haase, A., Landwehr, G., Umbach, E. (eds.) *Röntgen Centennial*, World Scientific, Singapore, p. 81.

Wang, T.J., Solanki, S.K., Curdt, W., Innes, D.E., Dammasch, I.E.: 2002, *Astrophys. J.* **574**, L101.

Wang, T.J., Solanki, S.K., Curdt, W., Innes, D.E., Dammasch, I.E., Kliem, B.: 2003, *Astron. Astrophys.* **402**, L17.

Warren, H.: 2005, *Astrophys. J. Suppl.* **157**, 147.

Warren, H., Doschek, G.A.: 2005, *Astrophys. J.* **618**, L157.

Williams, D.R., *et al.*: 2002, *Mon. Not. Roy. Astron. Soc.* **336**, 747.

Williams, D.R., Török, T., Démoulin, P., van Driel-Gesztelyi, L., Kliem, B.: 2005, *Astrophys. J.* **628**, L163.

Yokoyama, T., Akita, K., Morimoto, T., Inoue, K., Newmark, J.: 2001, *Astrophys. J.* **546**, L69.

Young, P.R., Del Zanna, G., Landi, E., Dere, K.P., Mason, H.E., Landini, M.: 2003, *Astrophys. J. Suppl.* **144**, 135.